# **Enzymatic Morphology Transformation Forms**

# **Intracellular Peptide Filaments**

Zhaoqianqi Feng,<sup>1,5</sup> Huaimin Wang,<sup>1,5</sup> Fengbin Wang,<sup>2</sup> Younghoon Oh<sup>3</sup>, Cristina Berciu<sup>4</sup>, Qiang Cui<sup>3,\*</sup>, Edward H. Egelman<sup>2,\*</sup>and Bing Xu<sup>1,6\*</sup>

- Department of Chemistry, Brandeis University, 415 South Street, Waltham,
  Massachusetts 02454, United States.
- 2. Department of Biochemistry and Molecular Genetics, University of Virginia, Box 800733, Charlottesville, VA 22908-0733.
- 3. Department of Chemistry, Boston University, 590 Commonwealth Avenue, Boston, Massachusetts 02215, MA 02478, United States.
- 4. Microscopy Core Facility, McLean Hospital, Belmont, MA 02478, United States.
- 5. These authors contributed equally.
- 6. Lead contact.

\*Correspondence: bxu@brandeis.edu; egelman@virginia.edu; qiangcui@bu.edu

# **Summary**

Intracellular protein filaments are ubiquitous for cellular functions, but forming bona fide biomimetic intracellular filaments of small molecules in living cells remains elusive. Here we report on the *in-situ* formation of self-limiting intracellular filaments of a small peptide via enzymatic morphological transition of a phosphorylated and trimethylated tetrapeptide. Enzymatic dephosphorylation reduces repulsive intermolecular electrostatic interactions and converts the peptidic nanoparticles into filaments, which exhibit distinct types of crossβ structures with either C7 or C2 symmetries, with the hydrophilic C-terminal residues at the periphery of the helix. Macromolecular crowding promotes the peptide filaments to form bundles, which extend from the plasma membrane to nuclear membrane and hardly interact with endogenous components, including cytoskeletons. Stereochemistry and post-translational modification (PTM) of peptides are critical for generating the intracellular bundles. This work may offer a way to gain lost functions or to provide molecular insights for understanding normal and aberrant intracellular filaments.

# **Key words**

Intracellular filaments; peptide filaments; self-assembly; filament structure; enzymatic reaction.

## Introduction

Noncovalent filaments of proteins are ubiquitous and play many critical roles in cells, such as myosin filaments for contraction, actin filaments for maintaining cell shapes, 2 microtubules for cell division,<sup>3</sup> and intermediate filaments for supporting nuclear envelop.<sup>4</sup> Moreover, filaments of aberrant proteins are known to associate with human diseases,<sup>5</sup> such as tau filaments of Alzheimer's diseases. Forming in the heterogenous, dynamic cellular environment, these protein filaments have stimulated the efforts to generate noncovalent filaments of synthetic molecules for understanding and mimicking the assembling behaviors and functions of the endogenous protein filaments. While using the self-assembly<sup>7</sup> of synthetic molecules (i.e., lipids<sup>8</sup>, saccharides<sup>9</sup>, peptides<sup>10-12</sup>) to form noncovalent filaments has been successful in vitro<sup>13-16</sup> or in well-confined conditions, the generation of intracellular filaments of synthetic molecules from self-assembly in living cells remains a challenge. Because cells are inherently out-of-equilibrium<sup>17</sup>, it is challenging to carry out self-assembly, a thermodynamic equilibrium process, of synthetic molecules inside cells. Moreover, the cytosol is dynamic, heterogenous, and highly crowded with proteins, 18 which would affect the self-assembly in a rather unpredicted manner.

One particularly promising class of self-assembling materials for mimicking protein structures and functions are peptides. Because of the versatile chemistry, relevance to biological signals, and programmable conformations, self-assemblies of peptides have

found applications in tissue engineering<sup>19</sup>, therapeutics<sup>20, 21</sup>, and bioimaging<sup>22</sup>. Despite the successful formation of filament of peptide *in vitro* and various applications *in vivo*, direct formation and real-time imaging of self-assembled filament of peptide in live cells is still extremely challenging. Moreover, the molecular understanding of the structures and dynamics of short peptides at very low concentration (0.2 mg/mL) in aqueous solution has yet to be achieved. Considering that the intracellular protein filaments are regulated by post-translational modification<sup>23</sup> and endogenous enzymatic reactions,<sup>24</sup> we have integrated self-assembly with enzymatic reaction as a biomimetic approach<sup>25, 26</sup> for controlling intermolecular interactions in complex environment, to create intracellular noncovalent filaments.

Here, we report the enzymatic formation of self-limiting intracellular filaments of a synthetic peptide (Scheme 1). Using cryo-EM, fluorescent microscopy, electron tomography, molecular dynamics, and molecular engineering, we elucidated the formation of intracellular filaments of a trimethylated tetrapeptide in live cells. The cryo-EM structural determination reveals that peptide self-assembles into two distinct types of cross-β structures that possess either C7 or C2 symmetries, as revealed by helical reconstructions using IHRSR.<sup>27</sup> Atomistic molecular dynamics simulations suggest that water and ions are present in the central pore of the filament and provide stabilization to the filament structure; MD simulations also find that phosphorylation of the peptide leads to reduced stability of the filament, agreeing with that filament formation requires dephosphorylation. Forming inside cells, the peptide filaments, exhibiting monodispersed diameters, pack as twist bundles and extend from the plasma membrane to nuclear membrane. Being orthogonal to endogenous cytoskeletons and hardly interacting with other endogenous components, the

filaments are cytoskeleton-like and able to impede cell migration. Cell-free experiment and coarse-grained molecular simulations support the macromolecular crowding enables the bundling of the filaments. Moreover, molecular engineering confirmed the importance of the stereochemistry and posttranslational modification (PTM) of peptides for forming intracellular bundles, which also underscores the inherent difference between *in vitro* and *in vivo* conditions. Using enzymatic morphological transition to generate artificial intracellular filaments of small molecules in a highly dynamic and crowded intracellular environment, this work may offer a way to gain lost functions of intermediate filaments<sup>28</sup> or to provide valuable insights for understanding pathogenic filaments of protein or peptides.

## Results

Molecular design and enzymatic morphological transition. The peptide, 1P-KMe<sub>3</sub> (Scheme 1), consists of a polarity sensitive fluorescent dye (nitrobenzoxadiazole (NBD)), a self-assembling D-peptide backbone (D-Phe-D-Phe),<sup>29</sup> a phosphatase cleavage site (D-phosphotyrosine), and a C-terminal trimethyl-L-lysine. Such a design allows alkaline phosphatase (ALP)<sup>30</sup> to convert 1P-KMe<sub>3</sub> to 1-KMe<sub>3</sub> (Figure 1a) and to initiate the self-assembly and morphological transition. We prepared the unnatural amino acids Fmoc-D-Tyr(PO<sub>3</sub>H<sub>2</sub>)-OH and Fmoc-Lys(Me)<sub>3</sub>-OH, and synthesized 1P-KMe<sub>3</sub> with Fmoc solid-phase peptide synthesis (SSPS)<sup>31</sup>. After using liquid chromatography to purify the crude product, we obtained 1P-KMe<sub>3</sub>. After being treated with ALP for 24 h in PBS buffer (pH 7.4), 1P-KMe<sub>3</sub> becomes dephosphorylated and turns into 1-KMe<sub>3</sub>. According to negatively stained TEM (Figure S1), while 1P-KMe<sub>3</sub> self-assembles to form nanoparticles around 15±3 nm, enzymatic dephosphorylation results in filaments with monodispersed

diameters around 6±1 nm. The partially aligned filament in the TEM images indicates that the interfilamental interactions favor the formation of bundles.

Structures of the filaments. To elucidate the structure of the filaments made of 1-KMe<sub>3</sub>, we used cryo-EM to determine the structure of these filaments (Figures 1a, S2). There are two types of filaments (types 1 and 2). The helical symmetries of both types of filaments were found by trial-and-error until recognizable peptide-like features were seen. Possible helical symmetries were calculated from the averaged power spectrum of boxed filaments (Figure 1b). Finally, the type 1 filaments were determined to have C7 symmetry (rise 4.9 Å, twist 2.3 degrees) while the type 2 filaments to have C2 symmetry (rise 4.9 Å, twist 2.7 degrees).

For the type 1 filament with C7 symmetry, we were able to reach ~4.3 Å resolution by helical reconstruction using IHRSR<sup>27</sup>, as judged by a model:map Fourier shell correlation (FSC) (Figure S3). The reconstructed fibril density shows 1-KMe<sub>3</sub> molecule stacked in a parallel cross-β structure (Figure 1c-e, Figure S4, Supplementary Movie 1). As shown in the CPK model (Figure 1f), extensive aromatic-aromatic interactions contribute to the self-assembly of 1-KMe<sub>3</sub>. With the N-terminal attached NBD motifs pointing to the center and the hydrophilic C-terminal residues (D-tyrosine and L-trimethyllysine) at the periphery of the helix, the hydrophobic residues (D-Phe-D-Phe) constitute the middle "rings" of the helix (Figure 1g). It is possible that water molecules are trapped in the center, but after imposing 7-fold symmetry this density is uninterpretable. An atomic model was built with cross-β restraints (Table S1). The model is most favorable as judged by the model:map real-space correlation coefficient (Figure S5), although at this resolution there is still some ambiguity of the EM map hand as well as the hydrogen bonds between cross-β layers.

For the type 2 filaments with C2 symmetry, we were able to reach  $\sim$ 5-6 Å resolution by helical reconstruction. The EM map clearly shows that each asymmetric unit has three 1-KMe<sub>3</sub> molecules (Figure S6) so it forms a pseudo C6 structure within one cross- $\beta$  layer. At such resolution, the ambiguity of EM map hand and the difficulties of many possible peptide orientations within the asymmetric unit prevent us from building a reliable atomic model.

Formation of intracellular filaments. NBD allows confocal laser scanning microscopy (CLSM) to directly visualize the formation of the filaments in vitro and in vivo.8 In vitro CLSM images show (Figure 2a) that the solution of 1P-KMe<sub>3</sub> (200 µM) contains a few fluorescent puncta in a largely dark background, suggesting that 1P-KMe<sub>3</sub> forms the loose nanoparticles, as revealed by TEM (Figure S1), which equilibrate with monomeric 1P-KMe<sub>3</sub> at this concentration. Upon the treatment of ALP (2 U/mL) over 24 h, the solution with scatter fluorescent spots transforms to a bright fibrous network of 1-KMe<sub>3</sub> (Figures S7, S8). This result confirms that 1P-KMe<sub>3</sub> and 1-KMe<sub>3</sub> are suitable for fluorescent imaging of the enzymatic formation of the peptide filaments. We next used CLSM to visualize the growth of filaments in live Saos-2 cells, an osteosarcoma cell line<sup>32</sup> that overexpresses tissue nonspecific alkaline phosphatase (ALPL). Being incubated with 1P-KMe<sub>3</sub> for 1 h, Saos-2 cells exhibit bright fluorescent droplets, which are likely made of nanoparticles of 1P-KMe<sub>3</sub> in the cytosol, but mostly near the cell membrane (Figure 2b). Although the detailed mechanism of the endocytosis of the nanoparticles of 1P-KMe<sub>3</sub> remains to be elucidated, we speculate that nanoparticles of 1P-KMe<sub>3</sub> are able to interact the ALP enriched in lipid rafts of the Saos2 cells, thus inducing caveolin-mediated endocytosis.<sup>33</sup> Moreover, the D-peptide backbone of 1P-KMe<sub>3</sub> prevents its proteolysis in

lysosomal environment for its eventually lysosome escape. From 1 h to 2 h, short fluorescent fibers start to grow from the edge of cells, indicating the transformation of the nanoparticles to the filaments in live cells. At 12 h incubation, a network of interconnecting nanofibers has developed in the cytoplasm of the cells (Supplementary Movie 2). From 12 h to 24 h, the density of the nanofibers increases considerably, (Figures 2b and 2c, Supplementary Movie 3) confirming the formation of intracellular filaments. Inhibiting the activity of the ALPL of Saos-2 cells by a known inhibitor (DQB)<sup>34</sup> prevents the formation of intracellular filaments and results in fluorescent droplets, which further diminish at a higher concentration of the inhibitor (Figures 2d, S9). To validate the enzymatic transformation in live cells, we quantified the conversion of 1P-KMe<sub>3</sub> to 1-KMe<sub>3</sub> after incubating the Saos-2 cell with 1P-KMe<sub>3</sub>. We found that 45 %, 60 %, 72 %, 83 %, and 91 % of 1P-KMe<sub>3</sub> molecules were dephosphorvlated after 0.5 h, 1 h, 2 h, 12 h, and 24 h incubation, respectively (Figure 2e). This result agrees with the gradual growth of the intracellular filaments (Figure 2b). After incubating the Saos-2 cells with fresh culture medium, the intracellular fibrous network dissociates (Figure 2f) to become a few fluorescent puncta, confirming that the intracellular filaments are noncovalent and formed by self-assembly. The above results confirm that enzymatic dephosphorylation converts the droplets in the cytosols to intracellular filaments overtime in live Saos-2 cells. These results, to the best of our knowledge, fill the gap of generating and direct visualizing intracellular artificial filaments in live cells.

The intracellular networks of the 1-KMe<sub>3</sub> filaments resemble the appearance of cytoskeletons. To examine their relationship with the endogenous cytoskeletal filaments, we performed immunofluorescent staining of major cytoskeletal protein filaments, such as

actin filaments, microtubules, and intermediate filaments (i.e., vimentin and lamin) after incubating the Saos-2 cells with 1P-KMe<sub>3</sub> for 24 h (Figures 3, S10). Despite forming microtubule-like radiating fibers from the perinuclear region towards the cell periphery, the 1-KMe<sub>3</sub> filaments hardly overlap with microtubules, indicating little interaction between the 1-KMe<sub>3</sub> filaments and the microtubules in the cells. Although exhibiting different spatial distribution patterns from that of the F-actin inside the cells, the presence of the 1-KMe<sub>3</sub> filaments in cytoplasm causes the aggregation of F-actin, suggesting that the 1-KMe<sub>3</sub> filaments likely increasing intracellular viscosity and indirectly disrupt the Factin dynamics, which play a role in cell motility<sup>35</sup>. Additionally, the 1-KMe<sub>3</sub> networks hardly co-localize with cytoplasmic intermediate filaments vimentin or nuclear intermediate filament lamin. These results suggest that the intracellular filament networks formed by 1-KMe<sub>3</sub> are orthogonal to the endogenous cytoskeleton filaments of the Saos-2 cells. Although it is hard to rule out completely the interaction between the 1-KMe<sub>3</sub> filaments and other proteins, the intracellular formation of the 1-KMe<sub>3</sub> filaments is driven by enzyme-instructed self-assembly than by association with other proteins.

Electron tomography of the intracellular filament bundles. Providing 3D organization of cellular fractionations, electron tomography (ET) allows for the investigation of cellular architecture of complexes and supramolecular assemblies with structural dynamics in their natural, cellular environment.<sup>36, 37</sup> To directly investigate the artificial filaments in the cellular environment and their cellular location, we acquired montages of overlapping, high-magnification TEM images of a whole Saos-2 cell after treating it with 1P-KMe<sub>3</sub> for 24 h and imaged with CLSM (Figure S11). In contrast to the case of the untreated Saos-2 cells (Figures 4a, S12), bundles of filaments appear abundantly inside the treated cells

(Figures 4b, S13-S15). Spreading from the plasma membrane to the nuclear membrane (Figure 4c), these bundles have a various diameter (35-130 nm) and length. The 3D electron tomographic reconstruction (Figure 4d) confirms that these bundles are made up of clusters of intertwining filaments, agreeing with the *in vitro* TEM results. The morphology and diameters of these bundles differ from those of cytoskeletons (25 nm microtubule fibers and closely packed parallel actin filaments). Extending through the entire cytoplasm, the 1-KMe<sub>3</sub> bundles of filaments are in proximity to but not in contact with different organelles (e.g., nucleus, endoplasmic reticulum, and mitochondria) (Figures S13-14). Moreover, compared with the small and few vacuoles in untreated Saos-2 cells (Figure S12), large endocytic vacuoles (Figures 4b, 4c, and S15) are scattered throughout the cytoplasm of the 1P-KMe<sub>3</sub> treated cells, indicating the formation of intracellular filaments involving endocytosis.<sup>38</sup>

Since the 1-KMe<sub>3</sub> filaments affect the actin dynamics, we employed a wound closure assay to determine their effect on altering cell motility (Figures S16, S17). While the control cells migrate significantly to cross the scratch, the cells treated with 1P-KMe<sub>3</sub> (200  $\mu$ M) hardly migrate, agreeing with the modulation of dynamics of F-actin. The addition of 1P-KMe<sub>3</sub> at a lower concentration (100  $\mu$ M), which is unable to form the intracellular filaments (Figure S18), scarcely affects the migration of the cells, further confirming that the 1-KMe<sub>3</sub> filaments impede the cell migration.

Forming bundles of the filaments due to crowding. Macromolecular crowding in cellular environments is known to promote protein aggregation and phase separation<sup>39,40</sup>. To mimic the crowding in cytoplasm, we added crowding agent polyethylene glycol (PEG, 20 kDa), which induces attractive interactions through depletion effects<sup>41</sup>, into the solution of 1P-

KMe<sub>3</sub>. In the presence of PEG, bundles of filaments were formed via enzyme-instructed assembly. The formation of bundles depends on the degree of crowding (or excluded volume); while the addition of 20 % and 10 % PEG (w/v) induces the thick bundles of filaments with an average diameter of  $56 \pm 12$  nm and  $45 \pm 10$  nm respectively, the presence of 5 % PEG (w/v) results in thinner bundles (28  $\pm$  6 nm) with randomly oriented single filaments. The effect of crowding on the formation of filament bundles is also studied by using coarse-grained (CG) molecular dynamics simulations. The results confirm that rigid filaments form thick bundles only in a highly crowded environment, as observed in experiments (Figure 5b), which correspond to the formation of filament bundles within crowded cellular environments (Figure 4). Details and discussions of the CG simulations are included in the Supporting Information (Note S3, S4). While there could be a kinetic effect that prevent these fibers from coming together, the helicity of the filament also contributes the self-limiting of the diameters of the bundles. 42 In addition, we note that the individual fiber features a slight twist as illustrated in Figure 1e. Therefore, it is conceivable that to maximize the interaction between two fibers, they are not aligned perfectly, which likely leads to packing defects that limit the growth of the bundle beyond specific size. Alternatively, fibers might undergo additional twist to maximize the interactions between fibers; the accumulation of such twisting strain will also limit the growth of the bundle.

Atomistic molecular dynamics simulations. Using the Cryo-EM structural model of the 1-KMe<sub>3</sub> filament, we conducted atomistic molecular dynamics simulations to further probe the intermolecular interactions and the effect of phosphorylation on the structural stability of the filament. An infinite filament is modeled with periodic boundary condition and solvated with explicit water molecules/ions using the CGenFF, Charmm36 protein force

fields, and Charmm-GUI<sup>43-45</sup>, molecular dynamics simulations are then conducted at the time scale of ~100 ns to probe the effect of tyrosine phosphorylation on the structural stability of the filament as well as the potential presence of water and ions in the core of the filament; the latter issue is particularly interesting because the electron density of the pore region is difficult to interpret at the current EM resolution. Additional simulation details are given in the Supporting Information.

During the MD simulation, the length of the filament increases due to thermal fluctuation and the structure becomes less ordered compared to the initial EM model (Figure 6a). The magnitude of length increases, and the rate of extension depends on the conformation of the peptide bond between NBD and the rest of the peptide as well as the phosphorylation state of the tyrosine residue. As discussed in more detail in the SI (Note S1, Figure S36), the filament that has the least extension features a trans peptide bond for the linkage between NBD and the rest of the unphosphorylated peptide. Analysis of neighboring peptide-peptide interactions (Figure S33, 34) suggests that both intra-layer and inter-layer peptide interactions are dominated by favorable van der Waals interactions and the magnitude of interaction is stronger for the inter-layer peptides due to favorable sidechain stacking interactions, whereas repulsive electrostatic interactions are observed between neighboring NBD moieties and adjacent methylated lysine residues. Therefore, the phosphorylation of tyrosine which further increases the apparent charge of the peptide leads to destabilized filament, which is manifested as substantially larger filament extension observed in the 1P-KMe<sub>3</sub> simulations (Figure 6b).

An interesting observation from the MD simulation is that a significant number of water molecules are absorbed in the filament (Figure 6d); as shown in SI (Figure S36), these

include water molecules initially placed in the central pore of the filament as well as water molecules that penetrate into the filament during the MD simulation (Figure 6c). This is not unexpected because the filament core is lined by a group of NBD moieties, which feature substantial dipoles that repel each other (Figure S33) and need to be stabilized by water molecules; in addition, the tyrosine sidechain and the C-terminal carboxylate can also be stabilized by water, providing additional driving force for water penetration into the filament (Note S2).

To test whether ions (e.g., Na<sup>+</sup>) can also occupy the filament core to provide further stabilization of the NBD moieties, we initiated independent simulations with different numbers of ions in the filament core (0.5 to 1 ion per peptide layer). During the simulation, some ions diffuse out of the filament (Figure S36) and only a modest number of ions remain in the interior of the filament (Figure 6c). Nevertheless, the number of water molecules adsorbed in the filament and thus the filament length extension is affected by the amount of ions (Figure 6b, d).

## Discussion

This work demonstrates a strategy to generate artificial intracellular filaments *via* enzyme-controlled intracellular morphological transition. Many works have reported the self-assembly or enzymatic self-assembly in well-controlled conditions. To the best of our knowledge, this is the first example to direct formation of self-limiting filaments of peptides inside live cells and observe their formation directly by CLSM and EM. Because of heterogeneity, dynamics, and protein crowding inside cells, using short peptide (<6) to mimic protein filaments, as a form of biomaterials, in live cells has been unsuccessful. It is rather unexpected that such uniform filaments form in cytosol, a highly sophisticated

and dynamic medium. Besides the enzymatic reactions, the formation of the intracellular bundles of filaments is controlled by multiple factors, such as the behaviors of the peptide assemblies, the stability of the peptides, PTM, and the activities of enzymes (or cell types) (Scheme S1 and Figure S19). For example, replacing trimethyl-L-lysine in 1P-KMe<sub>3</sub> to trimethyl-D-lysine generates 2P-KMe<sub>3</sub>, which only forms pericellular filament on Saos-2 cells (Figure S20). Incubating the 3P-KMe<sub>3</sub>, in which all the amino acid residues are Lenantiomers, with cells results in weak fluorescence on live cells, likely due to the proteolysis of the peptide (Figure S21). Although 2P-KMe<sub>3</sub> and 3P-KMe<sub>3</sub>, in the presence of PEG, both form bundles of filaments via enzyme-instructed assembly (Figure S22), none of them form intracellular filaments. This result highlights the inherent difference between the intracellular environment and cell-free condition. Moreover, removing the methylgroups from trimethyl-lysine (1P-K) disturbs the filaments structures and forms aggregates of nanoparticles (Figure S23). The requirement of methylation at lysine, a PTM, of the peptide for forming intracellular filaments is unexpected, but it indicates PTM as an important feature for designing peptide assemblies. In addition, we also treated 1P-KMe<sub>3</sub> with stromal cells (HS-5) and glioblastoma cells (T98G) and only observed fluorescent dots in the cytosol of these cells (Figures S24, S25), suggesting that the high expression of alkaline phosphatase inside Saos2 is essential for the formation of intracellular filaments. Notably, all the filaments formed by enzymatic dephosphorylation exhibit monodispersed diameters, suggestion enzymatic self-assembly likely is a mechanism used by nature to generate self-limiting nanostructures. 46

Considerable number of small peptides are known to form filaments (or nanofibers) *in vitro*, but the atomistic information of the molecular arrangement in the filament is limited. This

work reveals the molecular arrangement of short peptides in the filament at 4.3 Å resolution, representing a significant advance for understanding the molecular interactions that stabilize the filaments of ultrashort peptides. Atomistic molecular dynamics simulations further highlighted the importance of water and ions in the center of the filament to the structural stability. These results are valuable for designing peptide filaments for functions.

In the past, it is unsuccessful to generate intracellular filament bundles of small molecules using enzymatic reactions. This inability likely originates from two aspects: (i) before the enzymatic reaction, the small precursor molecules diffuse easily even in the crowded cytosol and (ii) after the enzymatic reaction, the small molecules become less soluble and is difficult to diffuse in the crowded cytosol to form large assemblies. The formation of nanoparticles by 1P-KMe<sub>3</sub> likely limits the diffusion of the precursors in the highly crowded cytosol prior to the dephosphorylation, thus resulting in high local concentration of 1-KMe<sub>3</sub> after the enzymatic reaction for the robust formation of the filaments. The transition from nanoparticles to filaments likely is resulted from successive enzymatic dephosphorylation. Such morphological transition allows artificial intracellular filaments to modulate intracellular viscosity.<sup>47</sup> This work also confirms that the essence of intracellular phase transition is enzymatic reaction(s), which agree with the use of enzymatic switch to control phase transition.<sup>48</sup> Although the distribution of molecular filaments in live cells is orthogonal to other cellular cytoskeletons, such filaments prevent the migration of cancer cells. Since cell migration is a key feature of metastasis that contributes to the failure of cancer therapy, this result underscores the potential applications

of the intracellular filaments in controlling cell mechanics<sup>49, 50</sup> or selectively targeting tumors<sup>20</sup>.

# **Experimental Procedures**

# **Resource Availability**

# **Lead Contact**

Further information and requests for resources and reagents should be directed to and will be fulfilled by the Lead Contact, Bing Xu (<u>bxu@brandeis.edu</u>).

# Materials Availability

All unique/stable reagents generated in this study are available from the Lead Contact with a completed Materials Transfer Agreement.

# **Data and Code Availability**

Data supporting the findings of this study are available within the paper and the <u>Supplemental Information</u> or are available from the Lead Contact upon reasonable request.

# Materials and synthesis

Descriptions of the materials, peptide synthesis and characterization are available in the Supplementary Information (Supplemental Experimental Procedures, Figure S26-29).

# Cryo-EM and image processing

After 6-time dilution, 4.5 μL of 1-KMe<sub>3</sub> sample was applied to discharged lacey carbon grids and plunge frozen using a Vitrobot Mark IV (FEI). Grids were imaged in a Titan Krios at 300 keV at NCI cryo-EM facility, and recorded with a K2 direct electron detector

at 1.06 Å per pixel, with 25 "fractions" per image. Each fraction represented a dose of  $\sim 2$ electrons/Å<sup>2</sup>. All the images were first motion corrected and dose weighted by MotionCorr v2.1 (23644547), and the first fraction were removed. Then a total of 1,107 images were selected that were free from drift or astigmatism, contained visible virus filaments, and had a defocus range from 0.5 to 3.0 µm determined by CTFFIND3 (12781660). The SPIDER software package (8742743) was used for subsequent steps. The CTF was corrected by multiplying each image by the theoretical CTF, both reversing phases where they need to be reversed and improving the signal-to-noise ratio. This multiplication of the images by the CTF is actually a Wiener filter in the limit of a very poor SNR. The program e2helixboxer within EMAN2 (16859925) was used for boxing long filaments from the micrographs. Overlapping 384-pixel long segments, with a 7 px shift between adjacent boxes (~1.5 times the axial rise per subunit) were extracted from these long filaments and then padded to 384 × 384 pixel (108,886 segments for type 1 filaments; 65,221 for type 2 filaments). The CTF determination and particle picking came from the integrated images (all 24 fractions after motion correction), while the segments used for the initial alignments and reconstruction came from the first 10 fractions accounting for a total dose of ~20 electrons/Å<sup>2</sup>. The determination of the helical symmetry was by trial and error, searching for a symmetry which yielded recognizable peptide-like feature. The IHRSR algorithm (11125866) was used for the helical reconstructions. The map was further sharpened using a negative B-factor of 100. The final resolution of the map was estimated by d<sub>99</sub> (30198894) and model:map FSC if a model is available.

# **Model building**

The atomic model of type 1 filament was built *de novo*. First, the map corresponding to a single cross-β layer was segmented from the filament density map in Coot (15572765). Then seven copies of the peptide molecules were manually docked into the density map and refined against the EM map using PHENIX (20124702). Two possible peptide orientation and two EM volume hands were considered, and the solution with the best real-space correlation coefficient (RSCC) was picked. Then a filament model was generated from this and then refined against the whole EM map. Four different restraints of the cross-β hydrogen bonds were screened, and the solution with the best RSCC was picked. The statistics are listed in Supplementary Table 1.

# **Confocal microscopy**

Saos-2 cells were seeded at  $1.5\times10^5$  cells in a 3.5 cm confocal dish for 24 hours to allow attachment. After incubating with 100 uM or 200  $\mu$ M 1P-KMe<sub>3</sub>, Saos-2 cells were washed with live cell image solution (Life Technologies A14291DJ) for 3 times and stained with 1.0  $\mu$ g/ml Hoechst 33342 for 10 min at 37 °C in dark. Finally, the cells were washed three times and kept in the live cell imaging solution for imaging using Zeiss LSM 880 confocal microscopy at the lens of 63× with oil.

# Immunofluorescence of cytoskeleton proteins

Saos-2 cells were seeded at  $1.5 \times 10^5$  cells in a 3.5 cm confocal dish for 24 hours to allow attachment. After incubating with 200  $\mu$ M 1P-KMe<sub>3</sub> for 24 h at 37 °C in a humidified atmosphere of 5% CO<sub>2</sub>, the cells were washed by PBS for three times, and then fixed by 4% formaldehyde for 15 min at 37 °C. Following three-time wash with PBS, the cells were incubated in 1% BSA/10% normal goat serum/0.3M glycine in 0.1% PBS-Tween for 1 h to permeate the cells and block non-specific protein-protein interactions. After another

three time wash by PBS buffer, the cells are treated with primary antibodies overnight at  $4\,^{\circ}$ C. The secondary antibody is (Alexa Fluor® 647 goat anti-rabbit (or mouse) IgG (H+L) used at the concentration of 2  $\mu$ g/ml for 1 h. Finally, Hochest 33342 was used to stain the cell nucleus.

# Cell sample preparation for transmission electron microscopy and electron tomography

The methods for TEM of cells and electron tomography used were performed as previously described<sup>51</sup>. Briefly, the cells were seeded on Aclar film discs of 1.5 mm diameter and 51 micrometers thick, mounted on a Lab-Tek II chambered cover glass using Matrigel. Before seeding the cells, the discs were UV sterilized and incubated in supplement-free McCoy's 5A medium for 2h. Then the Saos-2 cells were seeded at 2.0×10<sup>5</sup> cells, chosen to obtain 70–90% confluent cultures one day after seeding, in an incubator at 37 °C and 5% CO<sub>2</sub>. After 24 h, the cells were treated with 200 µM 1P-KMe<sub>3</sub> for 24 hours, while the control cells were treated with complete culture medium. Then the cells were washed with supplement-free culture medium and, imaged using Zeiss LSM 880 confocal microscopy. Then the Aclar discs with cells were quickly transferred into the aluminum platelets (type A) for high-pressure freezing, filled with 150 mM sucrose (as a cryoprotectant) in growing medium with no supplement, and covered with the flat side of another platelet (type B), creating a cavity of 0.1mm depth. Samples were rapidly frozen using a Leica HPM-100 high-pressure freezer (Leica Microsystems, Vienna, Austria). High pressure freezing was followed by freeze substitution using the Leica AFS-2 automatic freeze-substitution device. Dehydration and fixation occurred at low temperatures (starting at -90°C) over 5 days in a solution containing 1% osmium tetroxide, 0.5% anhydrous glutaraldehyde, and 2% water

in anhydrous acetone. Afterwards, the temperature was raised to 4°C, and cells on disks were infiltrated and embedded in EMbed 812/Araldite 502-Resin at RT. Polymerization of was done at 60 °C for a few days.

# Transmission electron microscopy of cells

Multiple ultrathin sections (of 70-80 nm) were cut on a Reichart Ultracut E, collected on Formvar coated copper slot grids, post-stained with uranyl acetate (saturated solution) and Reynold's lead citrate and initially imaged at a JEOL JEM-1200EX TEM with a 1k CCD camera (GATAN) in order to get overview maps of the sections, and localize the cells of interest. Then, for high resolution images of these cells, we imaged them at a 200 kV Tecnai F20 intermediate voltage TEM (FEI, Inc., Hillsboro, OR, USA) with a 4k CCD camera (GATAN), at 19,000X magnification (1.12 nm pixel size). For large overviews of the cells at medium magnification we acquired montages of overlapping images in an automated fashion using the microscope control software SerialEM<sup>52</sup>.

# **Electron tomography**

After collecting and analyzing TEM images, the grids with the sections/cells of interest were prepared for ET by coating both sides with 10-nm colloidal gold fiducials that was previously incubated for 30 min in 5% BSA<sup>53</sup>. We acquired dual-axis tilt series of the areas of interest by tilting the sample from –60° to +60°, with 1° increments using the microscope control software SerialEM<sup>52</sup> on a Tecnai F20 (200 keV) and the 2K × 2K CCD camera. Using the gold fiducial markers of the tilt series images in etomo from the IMOD software package <sup>54, 55</sup>, we generated 3D tomographic reconstructions, on which, later on, and we did 3D modeling of our structures of interest.

# Molecular dynamics simulation model and method

# All Atom Simulations

The cryo-EM structural model is used as the initial structure for the 1-KMe<sub>3</sub> fiber simulation. The fiber has approximately C<sub>7</sub> symmetry, and a small helical twist of ~2.34° per peptide; thus 22 layers of peptides are included such that periodic condition can be maintained along the filament axis across the boundary of unit cells (i.e. 22×2.34°~360°/7). The peptide is described with the CHARMM36m force field and the NBD moiety is described with CGenFF.<sup>56, 57</sup> The filament is solvated with TIP3P water and ions using CHARMM-GUI;<sup>58</sup> the ion concentration is close to be 0.15 M, which is the physiological condition. The initial simulation box is of dimension 14 × 14 × 10.8 nm³ and contain ~208K atoms. Gromacs simulation package is used for the atomistic simulations.<sup>59</sup> To explore the effect of phosphorylation on the structural stability of the fiber, we phosphorylate the Tyr residue in each peptide, leading to the 1P-KMe<sub>3</sub> simulation models. Since 1P-KMe<sub>3</sub> was observed not to form filaments in the experiment, we hypothesize that the 1P-KMe<sub>3</sub> fiber is structurally less stable in the simulations than the 1-KMe<sub>3</sub> fiber models.

Electrostatic interactions are calculated using particle-mesh-Ewald<sup>60</sup> with a grid size ~1 Å. Van der Waals interactions are calculated with force-switch with a cutoff distance of 1.2 nm and a switching distance of 1.0 nm. The Nose-Hoover thermostat<sup>61, 62</sup> and Parrinello-Rahman barostat<sup>63</sup> are used to control the temperature and pressure at 300 K and 1 bar, respectively. Semi-isotropic pressure coupling is used since the filament is continuous across the periodic boundary along the filament axis. Bonds with hydrogen are constrained

using the LINCS algorithm<sup>64</sup> to allow an integration time step of 2 fs. Three independent simulations are performed for all of the model filaments and the simulations are propagated for at least 120 ns (see Table S4).

The Cryo-EM structural model has the *cis* configuration for the peptide bond between NBD and the phenylalanine residue (Figure S30). The *cis* configuration for a peptide bond is rather unusual, although it has been observed near the end of a peptide. Nevertheless, since it is difficult to distinguish the *cis* from the common *trans* conformer at the EM resolution, we have also constructed a *trans* fiber model in which the *cis* peptide bond is rotated into the *trans* configuration. This is done by allowing other dihedral angles relevant to the NBD residue to adjust to avoid overlaps with other atoms.

As illustrated in Figure S31, adjusting the conformation of the first peptide bond leads to structural changes in the NBD moieties, which lean further downward compared to the EM structural model. As a result, the volume of the center cavity is slightly larger in the *trans* filament compared to the *cis* model. For example, when water molecules are introduced into the system, more water molecules ( $N_{wat} = 156$ ) are included for the *trans* fiber compared to the *cis* model ( $N_{wat} = 112$ ) with  $f_{ion} = 0$ .

Another technical detail concerns the placement of water and ions in the filament core. At the current EM resolution, the density of the core is difficult to interpret. Since the core is lined with NBD, which is highly polar, it is likely water and ions are present. Water molecules are introduced into the pore by superimposing water boxes at the bulk water density with the filament structure and removing water molecules within 2.8 Å from any protein atom. As to ions, we place a varying number of Na<sup>+</sup> ions in the core; this is characterized by f<sub>ion</sub>, the number of ion(s) per peptide layer, and we tested the values of 0,

0.5, 0.72 and 1.0. When ions are placed in the filament core, the same number of water is removed.

To investigate the favorable structure of the peptide in solution, we simulate a single *trans* peptide in solution up to 250 ns with four independent simulations and calculate Ramachandran plot for all four peptide bonds (Figure S32). The initial dihedral angles obtained from the Cryo-EM structure are marked as yellow star. As shown in the Figure S32, the equilibrium structure of peptide in solution is rather different from the Cryo-EM structure. Therefore, for the peptides to self-assemble into the highly ordered filaments, significant structural transition of individual peptides as well as the subtle balance between favorable inter-peptide interactions and unfavorable entropic loss are required.

# Coarse-grained Simulations

To investigate crowding effect on the bundling of filaments, we perform coarse-grained (CG) Langevin dynamics (LD) simulations by using a generic polymer model. The LAMMPS simulation package is used for the CG simulations<sup>65</sup>.

Each polymer chain is modeled as a bead-spring chain that is composed of 32 monomers of diameter  $\sigma$  and mass m; crowders are modeled as spherical particles of diameter 4  $\sigma$  and mass 64m. Neighboring monomers are connected by the harmonic bonding potential  $U_b(r) = k(r-r_0)^2$ , in which the reference distance  $r_0$  is set to 1.2  $\sigma$ . The force constant is taken to be  $k = 1000 \text{ k}_B \text{T/}\sigma^2$ , where  $k_B$  and T denote the Boltzmann constant and simulation temperature, respectively. The harmonic angular potential  $U_b(\theta) = k_{\text{angle}}(\theta-\theta_0)^2$  is also applied with a  $k_{\text{angle}}$  of 300  $k_B \text{T/}\theta_0^2$ , in which  $\theta_0 = \pi$ .

The non-bonded interactions between monomers of polymer are described by a truncated and shifted Lennard-Jones potential; the cut-off distance is 2.5  $\sigma$ . Other non-bonded interactions between polymer-crowder and crowder-crowder are taken to be purely repulsive and described by the Weeks-Chandler-Andersen (WCA) potential<sup>66</sup> with the same well-depth parameter  $\varepsilon$  as that for the polymer monomer-monomer interactions.

The Langevin dynamics (LD) simulations are conducted with the Velocity-Verlet integrator and an integration time step of 0.002  $\tau$ , where  $\tau$  is reduced time unit ( $\tau = (m\sigma/k_BT)^{0.5}$ ). All of our simulation box is cubic with a dimension  $L = 128 \ \sigma$ . Periodic boundary condition is applied to all directions. The number of polymer molecules is set to be 128. The volume fraction  $\rho$  of the crowder varies from 0.01 to 0.40, where  $\rho = (4/3) \ \pi$   $\sigma_c^3 \ N / L^3$  and N is the number of crowder particles.

# Acknowledgement

This research was, in part, supported by the National Cancer Institute's National Cryo-EM Facility at the Frederick National Laboratory for Cancer Research under contract HSSN261200800001E, and by NIH CA142746 (to B.X.), GM122510 (to E.H.E.), F99CA234746 (to Z.F.), and NSF DMR-1420382.

## **Author Contribution**

B. X., Z.F. and H.W. conceived the study. Z.F. and H.W., under the supervision of B. X., designed and performed the chemical synthesis, images of filaments in cell free and cell based assays, analyzed the experimental results. F.W., under the supervision of E.H.E., performed the image analysis, reconstructed the filament structure, generated, refined the

filament model. C.B., with the help of Z.F., performed sample preparation and data acquisition for electron microscopy images of cell samples. Y.O. and Q.C. performed computational modeling. B. X., Z.F. and H.W. wrote the manuscript with input from all authors.

# **Competing Interests**

The authors declare no competing financial interests.

# Reference

- J. Needham, A. Kleinzeller, M. Miall, M. Dainty, D. M. Needham, A. S. C. Lawrence. (1942).
  IS MUSCLE CONTRACTION ESSENTIALLY AN ENZYME-SUBSTRATE COMBINATION? Nature 150, 46-49.
- 2. F. van den Ent, L. A. Amos, J. Löwe. (2001). Prokaryotic origin of the actin cytoskeleton. Nature *413*, 39-44.
- 3. T. Mitchison, M. Kirschner. (1984). Dynamic instability of microtubule growth. Nature *312*, 237-242.
- 4. L. Gerace, G. Blobel. (1980). The nuclear envelope lamina is reversibly depolymerized during mitosis. Cell *19*, 277-287.
- 5. E. Chuang, A. M. Hori, C. D. Hesketh, J. Shorter. (2018). Amyloid assembly and disassembly. J Cell Sci *131*, jcs189928.
- 6. A. W. P. Fitzpatrick *et al.* (2017). Cryo-EM structures of tau filaments from Alzheimer's disease. Nature *547*, 185-190.
- 7. G. M. Whitesides, B. Grzybowski. (2002). Self-assembly at all scales. Science *295*, 2418-2421.
- 8. S. Onogi, H. Shigemitsu, T. Yoshii, T. Tanida, M. Ikeda, R. Kubota, I. Hamachi. (2016). In situ real-time imaging of self-sorted supramolecular nanofibres. Nat. Chem. *8*, 743-752.
- 9. S. S. Lee *et al.* (2017). Sulfated glycopeptide nanostructures for multipotent protein activation. Nat. Nanotechnol. *12*, 821-829.
- M. Kumar, N. L. Ing, V. Narang, N. K. Wijerathne, A. I. Hochbaum, R. V. Ulijn. (2018).
  Amino-acid-encoded biocatalytic self-assembly enables the formation of transient conducting nanostructures. Nat. Chem. 10, 696-703.
- 11. E. R. Draper, E. G. B. Eden, T. O. McDonald, D. J. Adams. (2015). Spatially resolved multicomponent gels. Nat. Chem. *7*, 849-853.
- 12. D. D. Wu *et al.* (2019). Polymers with controlled assembly and rigidity made with click-functional peptide bundles. Nature *574*, 658-662.
- 13. S. Bera, S. Mondal, B. Xue, L. J. W. Shimon, Y. Cao, E. Gazit. (2019). Rigid helical-like assemblies from a self-aggregating tripeptide. Nat. Mater. *18*, 503-509.
- 14. H. Cui, E. T. Pashuck, Y. S. Velichko, S. J. Weigand, A. G. Cheetham, C. J. Newcomb, S. I. Stupp. (2010). Spontaneous and X-ray-triggered crystallization at long range in self-assembling filament networks. Science *327*, 555-559.

- 15. P. W. J. M. Frederix, G. G. Scott, Y. M. Abul-Haija, D. Kalafatovic, C. G. Pappas, N. Javid, N. T. Hunt, R. V. Ulijn, T. Tuttle. (2015). Exploring the sequence space for (tri-)peptide self-assembly to design and discover new hydrogels. Nat. Chem. 7, 30-37.
- 16. T. O. Omosun *et al.* (2017). Catalytic diversity in self-propagating peptide assemblies. Nat. Chem. *9*, 805-809.
- 17. C. P. Brangwynne, P. Tompa, R. V. Pappu. (2015). Polymer physics of intracellular phase transitions. Nat. Phys. *11*, 899-904.
- 18. C. M. Dobson. (2004). Chemical space and biology. Nature *432*, 824-828.
- 19. D. J. Smith *et al.* (2016). A multiphase transitioning peptide hydrogel for suturing ultrasmall vessels. Nat. Nanotechnol. *11*, 95-102.
- 20. Z. Feng, X. Han, H. Wang, T. Tang, B. Xu. (2019). Enzyme-Instructed Peptide Assemblies Selectively Inhibit Bone Tumors. Chem *5*, 2442-2449.
- 21. G. A. Hudalla, T. Sun, J. Z. Gasiorowski, H. F. Han, Y. F. Tian, A. S. Chong, J. H. Collier. (2014). Gradated assembly of multiple proteins into supramolecular nanomaterials. Nat. Mater. 13, 829-836.
- 22. G. L. Liang, H. J. Ren, J. H. Rao. (2010). A biocompatible condensation reaction for controlled assembly of nanostructures in living cells. Nat. Chem. *2*, 54-60.
- 23. N. T. Snider, M. B. Omary. (2014). Post-translational modifications of intermediate filament proteins: Mechanisms and functions. Nat. Rev. Mol. Cell Biol. *15*, 163-177.
- 24. A. Desai, T. J. Mitchison. (1997). Microtubule polymerization dynamics. Annual Review of Cell and Developmental Biology *13*, 83-117.
- 25. Z. Yang, H. Gu, D. Fu, P. Gao, J. K. Lam, B. Xu. (2004). Enzymatic formation of supramolecular hydrogels. Adv. Mater. *16*, 1440-1444.
- 26. B. H. Hu, P. B. Messersmith. (2003). Rational design of transglutaminase substrate peptides for rapid enzymatic formation of hydrogels. J. Am. Chem. Soc. *125*, 14298-14299.
- 27. E. H. Egelman. (2014). Ambiguities in helical reconstruction. Elife, e04969.
- 28. M. B. Omary, P. A. Coulombe, W. H. I. McLean. (2004). Intermediate filament proteins and their associated diseases. N. Engl. J. Med. *351*, 2087-2100.
- 29. M. Reches, E. Gazit. (2003). Casting metal nanowires within discrete self-assembled peptide nanotubes. Science *300*, 625-627.
- 30. J. L. Millán, *Mammalian alkaline phosphatases: from biology to applications in medicine and biotechnology.* (John Wiley & Sons, 2006).
- 31. R. B. Merrifield. (1963). Solid Phase Peptide Synthesis. I. The Synthesis of a Tetrapeptide. J. Am. Chem. Soc. *85*, 2149-2154.
- 32. S. B. Rodan, Y. Imai, M. A. Thiede, G. Wesolowski, D. Thompson, Z. Barshavit, S. Shull, K. Mann, G. A. Rodan. (1987). Characterization of a human osteosarcoma cell line (Saos-2) with osteoblastic properties. Cancer Res. *47*, 4961-4966.
- 33. R. G. Parton, B. Joggerst, K. Simons. (1994). Regulated internalization of caveolae. J. Cell Bio. *127*, 1199-1215.
- 34. R. Dahl *et al.* (2009). Discovery and Validation of a Series of Aryl Sulfonamides as Selective Inhibitors of Tissue-Nonspecific Alkaline Phosphatase (TNAP). J. Med. Chem. *52*, 6919-6925.
- 35. T. D. Pollard. (2003). The cytoskeleton, cellular motility and the reductionist agenda. Nature *422*, 741-745.
- 36. V. Lucic, F. Forster, W. Baumeister. (2005). Structural studies by electron tomography: From cells to molecules. Annu. Rev. Biochem. *74*, 833-865.
- 37. M. J. Lee *et al.* (2018). Engineered synthetic scaffolds for organizing proteins within the bacterial cytoplasm. Nat. Chem. Biol. *14*, 142-147.

- 38. J. Huotari, A. Helenius. (2011). Endosome maturation. EMBO J. 30, 3481-3500.
- 39. R. J. Ellis. (2001). Macromolecular crowding: Obvious but underappreciated. Trends Biochem. Sci. *26*, 597-604.
- 40. S. S. Ribeiro, N. Samanta, S. Ebbinghaus, J. C. Marcos. (2019). The synergic effect of water and biomolecules in intracellular phase separation. Nat. Rev. Chem. *3*, 552-561.
- 41. H. X. Zhou, G. Rivas, A. P. Minton. (2008). Macromolecular crowding and confinement: Biochemical, biophysical, and potential physiological consequences. Annual Review of Biophysics *37*, 375-397.
- 42. D. M. Hall, I. R. Bruss, J. R. Barone, G. M. Grason. (2016). Morphology selection via geometric frustration in chiral filament bundles. Nat. Mater. *15*, 727-732.
- 43. K. Vanommeslaeghe *et al.* (2010). CHARMM General Force Field: A Force Field for Drug-Like Molecules Compatible with the CHARMM All-Atom Additive Biological Force Fields. J. Comput. Chem. *31*, 671-690.
- 44. J. Huang, S. Rauscher, G. Nawrocki, T. Ran, M. Feig, B. L. de Groot, H. Grubmuller, A. D. MacKerell. (2017). CHARMM36m: an improved force field for folded and intrinsically disordered proteins. Nat. Methods *14*, 71-73.
- 45. S. Jo, T. Kim, V. G. Iyer, W. Im. (2008). Software news and updates CHARNIM-GUI: A webbased grraphical user interface for CHARMM. J. Comput. Chem. *29*, 1859-1865.
- 46. Y. Xia, T. D. Nguyen, M. Yang, B. Lee, A. Santos, P. Podsiadlo, Z. Tang, S. C. Glotzer, N. A. Kotov. (2011). Self-assembly of self-limiting monodisperse supraparticles from polydisperse nanoparticles. Nature Nanotechnology *6*, 580-587.
- 47. H. Nakamura *et al.* (2018). Intracellular production of hydrogels and synthetic RNA granules by multivalent molecular interactions. Nat Mater *17*, 79-89.
- 48. Z. Yang, G. Liang, L. Wang, B. Xu. (2006). Using a Kinase/Phosphatase Switch to Regulate a Supramolecular Hydrogel and Forming the Supramolecular Hydrogel in vivo. J. Am. Chem. Soc. *128*, 3038-3043.
- 49. D. A. Fletcher, D. Mullins. (2010). Cell mechanics and the cytoskeleton. Nature *463*, 485-492.
- 50. J. Geng, W. Li, Y. Zhang, N. Thottappillil, J. Clavadetscher, A. Lilienkampf, M. Bradley. (2019). Radical polymerization inside living cells. Nat. Chem. *11*, 578-586.
- 51. Y. Gao, C. Berciu, Y. Kuang, J. F. Shi, D. Nicastro, B. Xu. (2013). Probing Nanoscale Self-Assembly of Nonfluorescent Small Molecules inside Live Mammalian Cells. Acs Nano *7*, 9055-9063.
- 52. D. N. Mastronarde. (2005). Automated electron microscope tomography using robust prediction of specimen movements. Journal of Structural Biology *152*, 36-51.
- 53. C. V. Iancu *et al.* (2006). Electron cryotomography sample preparation using the Vitrobot. Nature Protocols *1*, 2813-2819.
- J. R. Kremer, D. N. Mastronarde, J. R. McIntosh. (1996). Computer visualization of three-dimensional image data using IMOD. Journal of Structural Biology *116*, 71-76.
- 55. D. N. Mastronarde. (1997). Dual-axis tomography: An approach with alignment methods that preserve resolution. Journal of Structural Biology *120*, 343-352.
- 56. K. Vanommeslaeghe *et al.* (2010). CHARMM general force field: A force field for drug-like molecules compatible with the CHARMM all-atom additive biological force fields. J. Comput. Chem. *31*, 671-690.
- 57. J. Huang, S. Rauscher, G. Nawrocki, T. Ran, M. Feig, B. L. De Groot, H. Grubmüller, A. D. MacKerell, Jr. (2016). CHARMM36m: An improved force field for folded and intrinsically disordered proteins. Nat. Methods *14*, 71-73.

- 58. S. Jo, T. Kim, V. G. Iyer, W. Im. (2008). CHARMM-GUI: A web-based graphical user interface for CHARMM. J. Comput. Chem. *29*, 1859-1865.
- 59. M. J. Abraham, T. Murtola, R. Schulz, S. Páll, J. C. Smith, B. Hess, E. Lindah. (2015). Gromacs: High performance molecular simulations through multi-level parallelism from laptops to supercomputers. SoftwareX *1-2*, 19-25.
- 60. T. Darden, D. York, L. Pedersen. (1993). Particle mesh Ewald: An N·log(N) method for Ewald sums in large systems. The Journal of Chemical Physics *98*, 10089-10092.
- 61. S. Nosé. (1984). A unified formulation of the constant temperature molecular dynamics methods. The Journal of Chemical Physics *81*, 511-519.
- 62. W. G. Hoover. (1985). Canonical dynamics: Equilibrium phase-space distributions. Phys Rev A Gen Phys *31*, 1695-1697.
- 63. M. Parrinello, A. Rahman. (1980). Crystal Structure and Pair Potentials: A Molecular-Dynamics Study. Physical Review Letters *45*, 1196-1199.
- 64. B. Hess, H. Bekker, H. J. C. Berendsen, J. G. E. M. Fraaije. (1997). LINCS: A linear constraint solver for molecular simulations. J. Comput. Chem. *18*, 1463-1472.
- 65. S. Plimpton. (1995). Fast parallel algorithms for short-range molecular dynamics. J. Comput. Phys. *117*, 1-19.
- 66. J. D. Weeks, D. Chandler, H. C. Andersen. (1971). Role of repulsive forces in determining the equilibrium structure of simple liquids. The Journal of Chemical Physics *54*, 5237-5247.

# Figure titles and legends

**Scheme 1.** Schematic illustration shows the intracellular conversion of the nanoparticles of 1P-KMe<sub>3</sub> to bundles of intracellular filaments of 1-KMe<sub>3</sub> *via* enzymatic morphological transition, the molecular structures of 1P-KMe<sub>3</sub> and 1-KMe<sub>3</sub>, and the cryo-EM construction, and molecular dynamics simulations of peptide filament of 1-KMe<sub>3</sub>.

Figure 1. Structure and intermolecular interactions of the peptide filaments of 1-

# **KMe**<sub>3</sub>. a, A cryo-EM image of type 1 (yellow arrow) and type 2 (red arrow) 1-KMe<sub>3</sub> filaments. b, Average power spectra of type 1 filaments of 1-KMe<sub>3</sub>. c, 3D reconstruction of type 1 filaments of 1-KMe<sub>3</sub> from cryo-EM images. d, Atomic model of the type 1 fibril with cross-β structure. e, Top views of the cross section of the EM density of type 1 filament and the stick representation of the peptides. f and g, CPK model and chemical

structures of one layer of the filament at the cross section (e).

**Figure 2. Formation of the intracellular filaments**. a, CLSM images of nanostructures formed before and after adding ALP (2 U/mL) to the solution of 1P-KMe<sub>3</sub> (200 μM). Scale bars, 5 μm. b, CLSM images of Saos-2 cells treated with 1P-KMe<sub>3</sub> (200 μM) at different time. Scale bars, 10 μm. c, Three-dimensional CLSM image of Saos-2 cells treated with 1P-KMe<sub>3</sub> (200 μM) for 12 h or 24h. d, CLSM images of Saos-2 cells treated with 1P-KMe<sub>3</sub> (200 μM) and co-incubated with ALPL inhibitor (DQB) for 24 h. Scale bars, 10 μm. e, Percentage of 1P-KMe<sub>3</sub> remaining after treating with Saos-2 cells over the time course of 24 h. f, CLSM images of Saos-2 cells treated with 1P-KMe<sub>3</sub> (200 μM) for 12 h then incubated with fresh culture medium for 24 h. Scale bars, 10 μm.

Figure 3. The networks of the synthetic peptide filament being orthogonal to cytoskeletons. Immunofluorescent images (antibody staining for cytoskeleton proteins (red)) of the Saos-2 cells incubated with 1P-KMe<sub>3</sub> (200 μM) for 24 h. Scale bars, 10 μm.

**Figure 4. Electron microscopy images of the filament bundles of the peptide (1-KMe<sub>3</sub>) inside the cells.** a, TEM image of a whole Saos-2 cell (wild-type, untreated) and higher magnification electron micrograph of the red boxed area. b, TEM image of a treated Saos-2 cell (1P-KMe<sub>3</sub> 200 μM, 24h) and higher magnification electron micrographs of the red boxed area and the blue boxed area. c, TEM image of another treated Saos-2 cell (1P-KMe<sub>3</sub> 200 μM, 24h) and higher magnification electron micrograph of the red boxed area. d, 3D reconstruction models of the filament bundles (green), microtubules (pink) and nuclear envelope (blue) on an electron tomographic image of the blue boxed area in (c). Solid red arrowheads indicate bundles of artificial filament; N: nucleus; M: mitochondria; Act: actin; V: vacuoles; Mt: microtubules; NE: nuclear envelope. Scale bars in a, b, c, 2000 nm; in the boxed area in a, b, c, 500 nm; in d, 250 nm.

Figure 5. Formation of bundles of filaments in crowded environments. a, TEM image of nanostructures formed after adding ALP (2 U/mL) to the solution of 1P-KMe<sub>3</sub> (200  $\mu$ M) for 24 h, in the presence of 0 %, 5 %, 10 %, and 20 % (w/v) PEG 20000. Scale bar = 100 nm. b, MD simulation snapshots of coarse-grained model with different volume fractions

of crowders. Thick filament bundles are only observed in highly crowded environment.

**Figure 6. All-atom molecular dynamics (MD) simulations.** a. Initial structure and a snapshot after 50 ns of MD simulation of the 1-KMe<sub>3</sub> filament with  $f_{ion} = 0.5$ ;  $f_{ion}$  specifies the number of ions per layer of peptide orthogonal to the filament axis. Water and ions are omitted for clarity and black bars represent periodic boundary of the simulation box. b. Elongated length of the filament after 150 ns of MD simulation for different systems (1-KMe<sub>3</sub> and 1P-KMe<sub>3</sub> with different number of placed ions in the filament core). c. Distribution of water (red) and cations (yellow) within the filament (grey) in the initial structure and a snapshot after 50 ns of MD simulation of the 1-KMe<sub>3</sub> filament with  $f_{ion} = 0.5$ . d. The number of water molecules that are maintained within the filament at the end of 150 ns of MD simulation for different systems. The error bars in panels b and d are

obtained using the last ten nanoseconds of three independent 170 ns MD simulations.

# Supplemental video titles and legends

# Movie S1

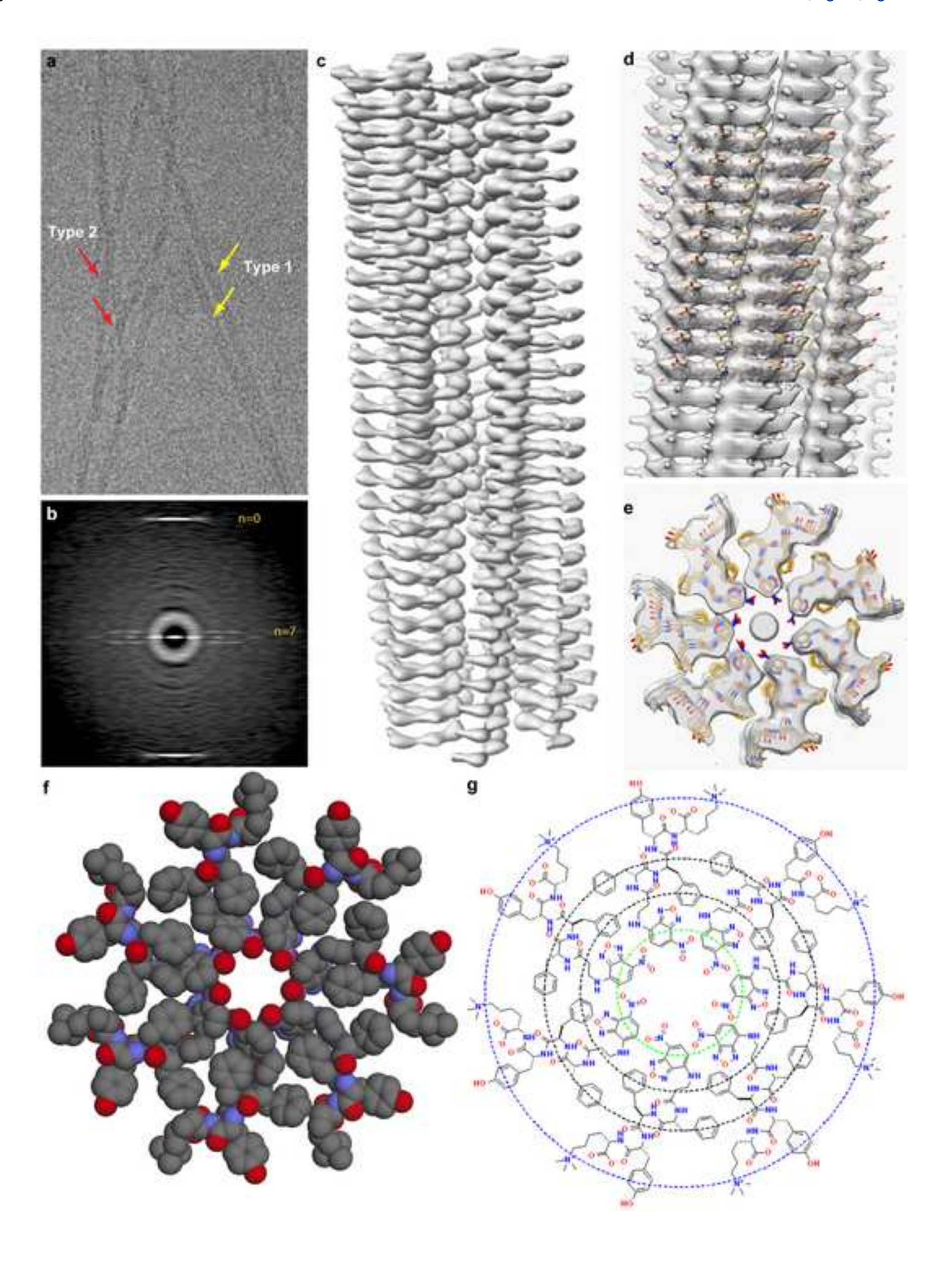
Established model 1 of cryo-EM structure of type 1 1-KMe<sub>3</sub> filament.

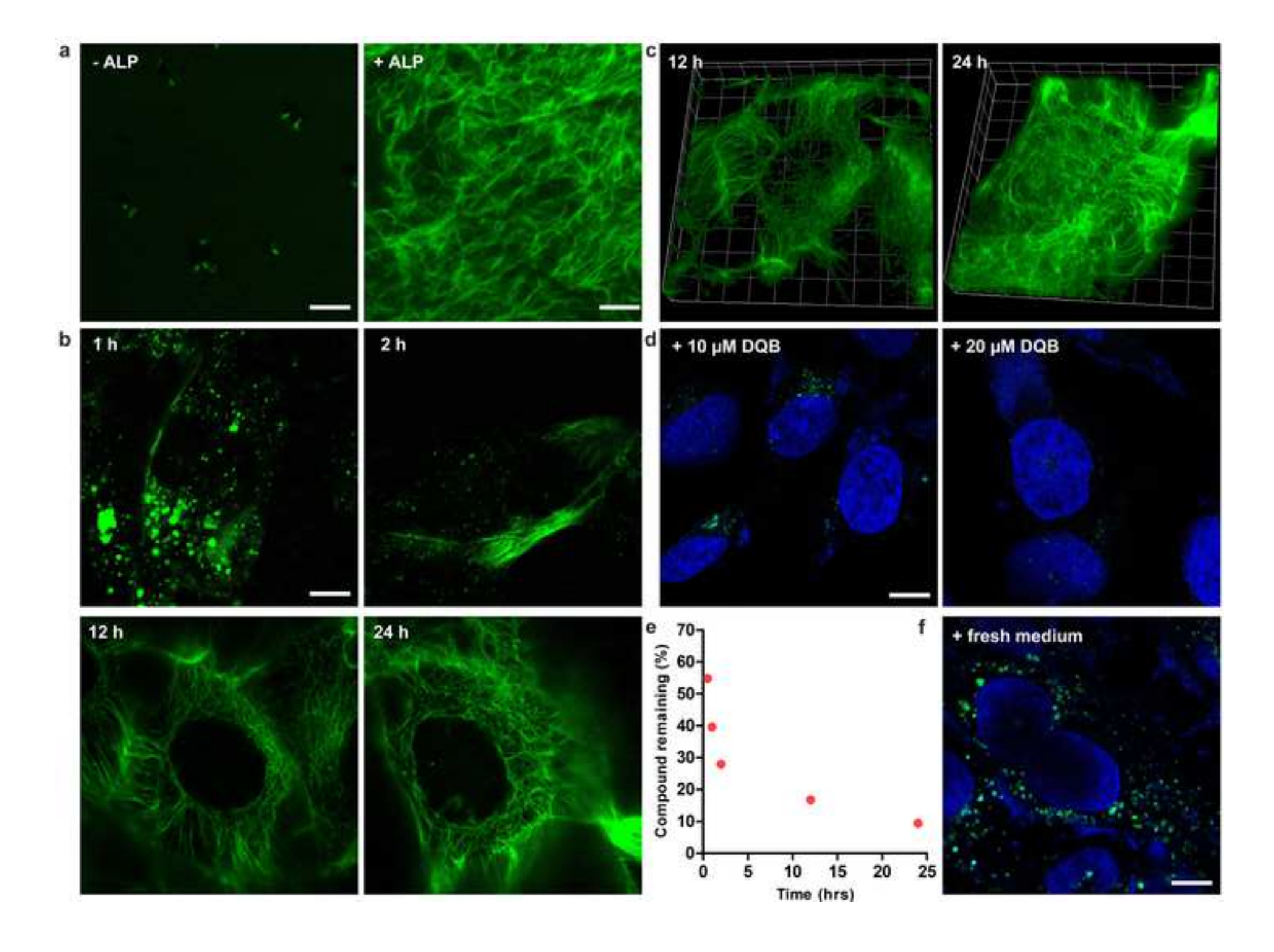
# Movie S2

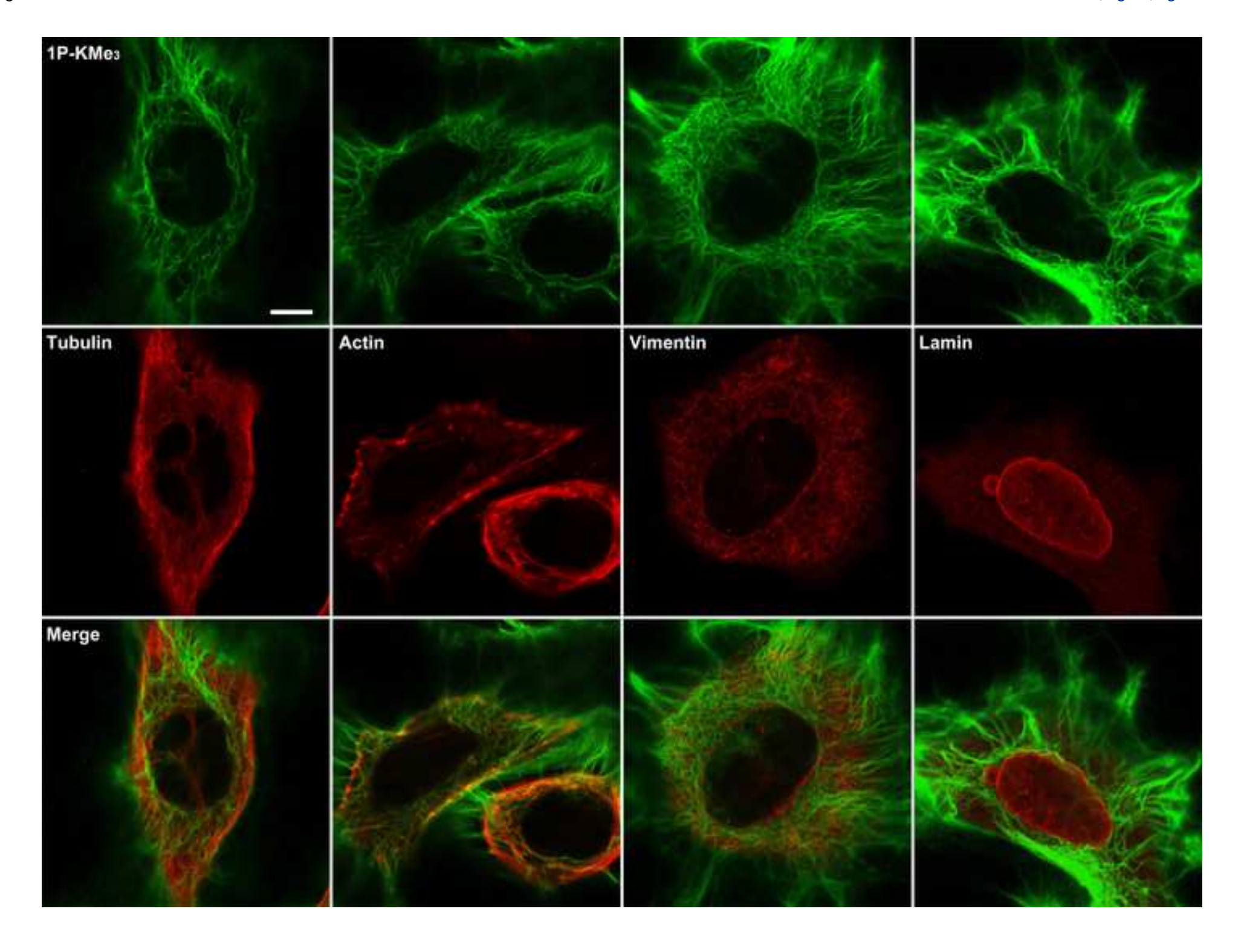
3D construction of Saos-2 cells incubated with 1P-KMe3 (200 μM) for 12 h.

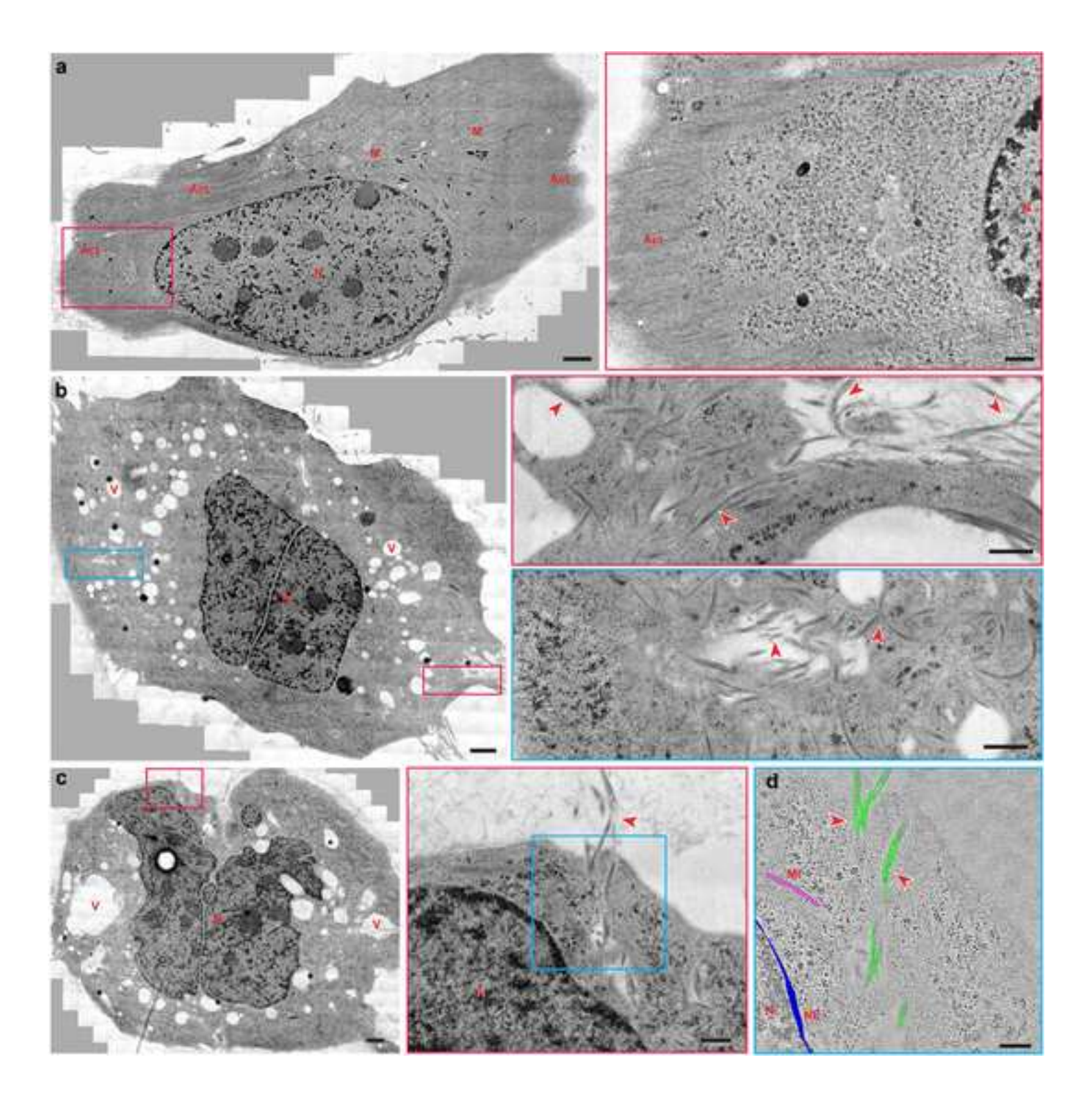
# Movie S3

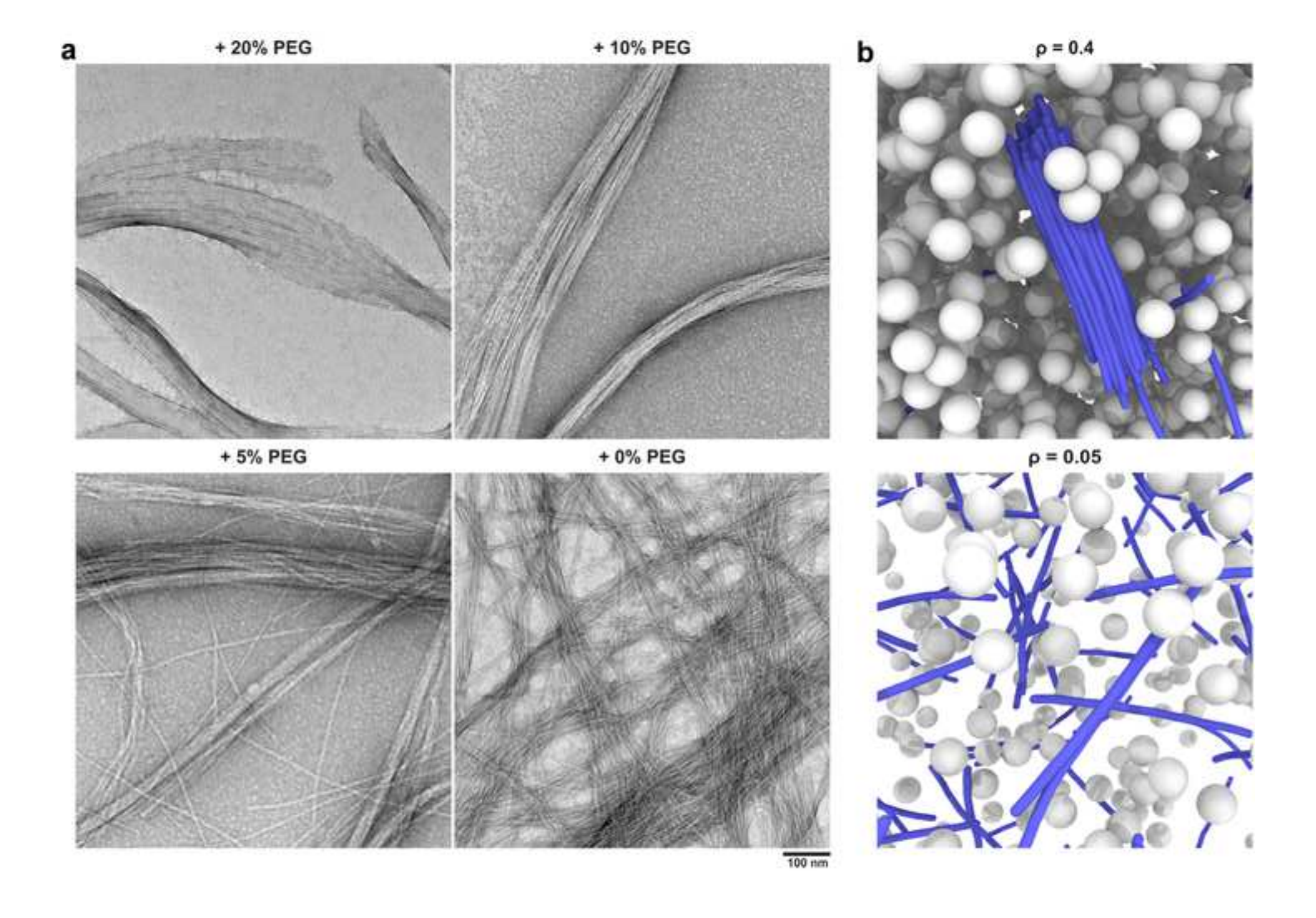
3D construction of Saos-2 cells incubated with 1P-KMe3 (200  $\mu M)$  for 24 h.

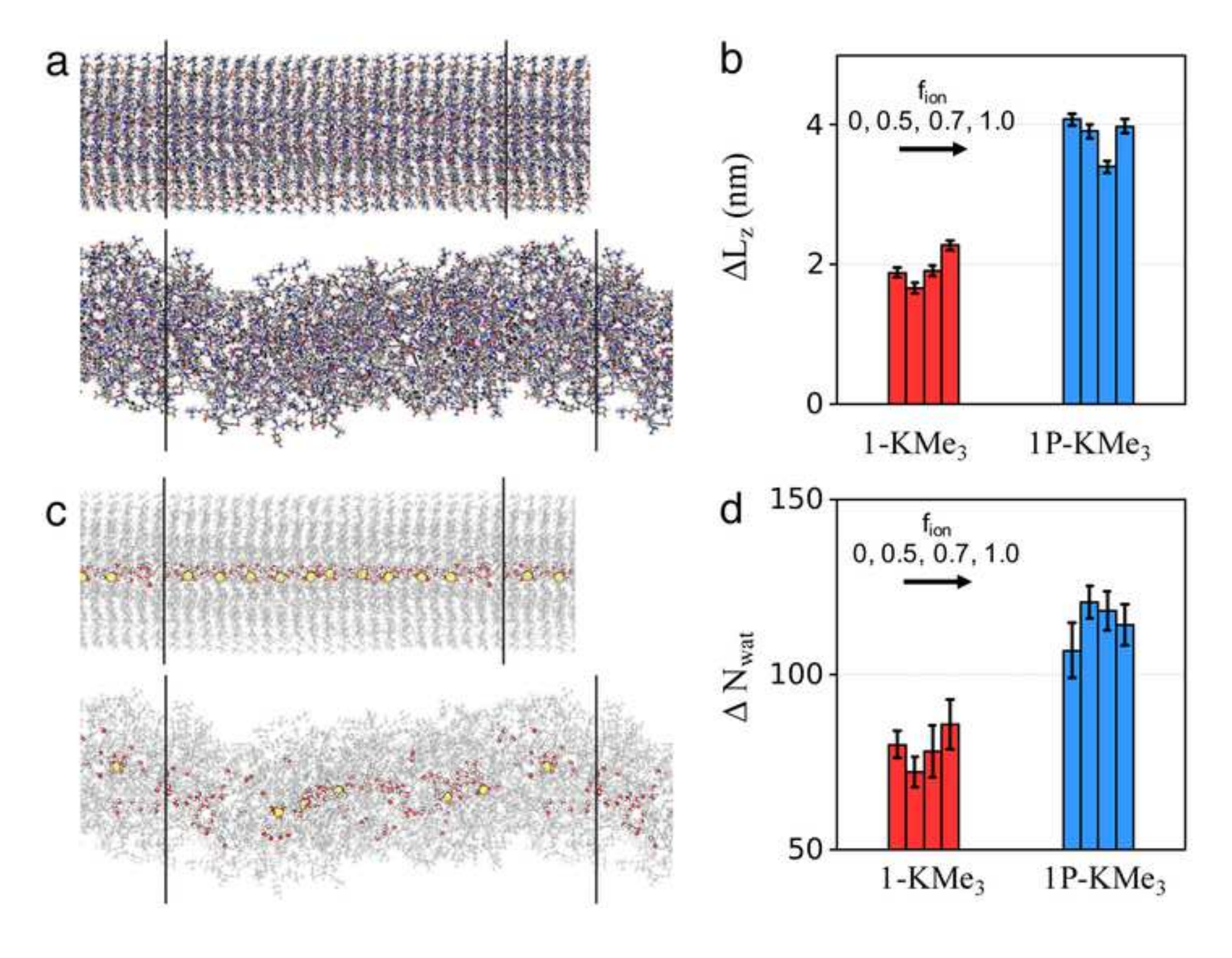


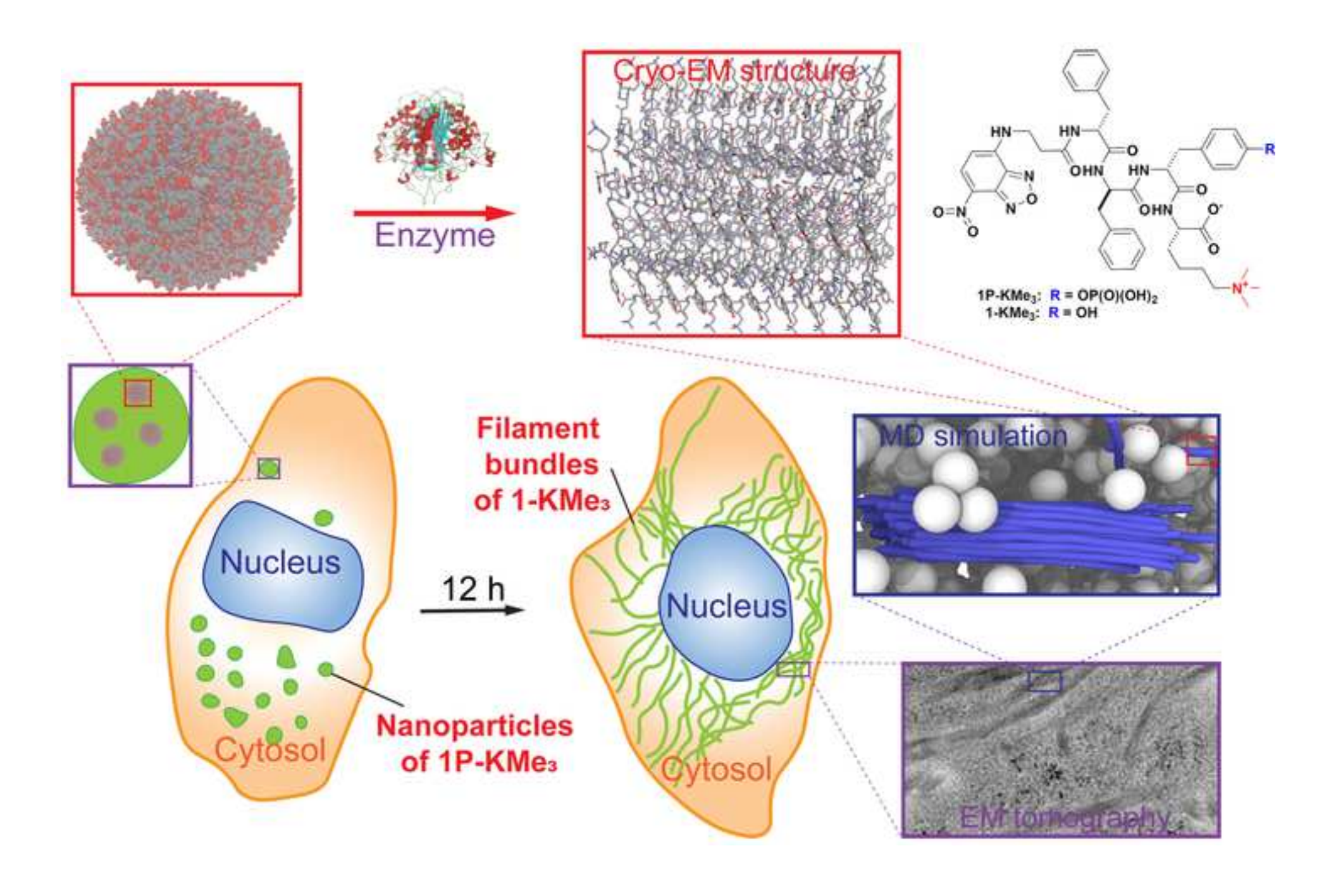












## **Supplemental Experimental Procedures**

#### Materials

2-Cl-trityl chloride resin (0.8-1.0 mmol/g), Fmoc-amino acids and HBTU were purchased from GL Biochem (Shanghai, China), and other chemical reagents and solvents were purchased from Fisher Scientific. Alkaline phosphatase was purchased from Biomatik (Cat. No. A1130), McCoy's 5A Medium, Minimum Essential Medium (MEM), Dulbecco's Modified Eagle Medium (DMEM), fetal bovine serum (FBS) and penicillin-streptomycin from Gibco by Life Technologies. LC-MS spectra were recorded with a Waters Acquity Ultra Performance LC with Waters MICROMASS detector. TEM images were obtained with Morgagni 268 transmission electron microscope and confocal laser scanning microscopy (CLSM) images with Zeiss LSM 880 confocal microscopy at the lens of 63× with oil. Carbon-coated copper grids (400 meshes) from SPI Supplies.

## Peptide synthesis and purification

All the peptides were synthesized with standard solid-phase peptide synthesis (SPPS) on 2-chlorotrityl chloride resin. Unnatural amino acids Fmoc-D-Tyr(PO<sub>3</sub>H<sub>2</sub>)-OH, and Fmoc-Lys(Me)<sub>3</sub>-OH were incorporated into the sequences as indicated. The synthetic protocol of Fmoc-D-Tyr(PO<sub>3</sub>H<sub>2</sub>)-OH, Fmoc-Lys(Me)<sub>3</sub>-OH were successfully synthesized according to literature procedures. Pollowing synthesis, the N-terminal of peptides were capped with NBD- $\beta$ -alanine which is synthesized based on previous report. The peptides were cleaved using 95% of trifluoroacetic acid with 2.5% of triisopropyl silane and 2.5% of H<sub>2</sub>O for 1 h. 20 mL per gram of resin of ice-cold diethyl ether was then added to cleavage reagent to yield yellow precipitate. The peptides were purified using Agilent 1100 Series Liquid Chromatograph system, equipped with a Variable Wavelength Detector and XTerra C18 RP column, using a water/acetonitrile gradient (20-100% acetonitrile over 30 min) with 0.1% trifluoroacetic acid.

## Transmission electron microscopy

 $5~\mu L$  of sample solution was placed to the carbon-coated copper grids after discharging by Glow Discharge Cleaning System. The sample was negative stained with uranyl acetate solution (2%, w/v) for three times per 15 seconds, then imaged using Morgagni 268 transmission electron microscope at the HV of 80 KV.

## **Cell culture**

Saos-2, HS-5, and T98G cells were purchased from American Type Culture Collection (ATCC, USA). Saos-2 cells were cultured in McCoy's 5A Medium (Gibco, Life Technologies) supplemented with 15% (v/v) fetal bovine serum (FBS) (Gibco, Life Technologies), T98G cells were cultured in Minimal Essential Medium (MEM) supplemented with 10% v/v FBS, and HS-5 cells were cultured in Dulbecco's Modified Eagle Medium (DMEM) supplemented with 10% v/v FBS. All culture mediums were supplemented with 100 U/mL penicillin and 100 μg/mL streptomycin (Gibco, Life Technologies) and all cells were maintained in a humidified atmosphere of 5% CO<sub>2</sub> at 37 °C.

## Determination of dephosphorylation rate in live cells

Saos-2 cells were seeded at  $1.5 \times 10^5$  cells in a 3.5 cm dish for 24 hours to allow attachment. After incubating with 200  $\mu$ M compounds for different time, the medium and cells were collected, dried, and redissolved in methanol. Finally, LC-MS was used to analyze the dephosphorylation and degradation of the compounds.

## **Supplemental Figures**

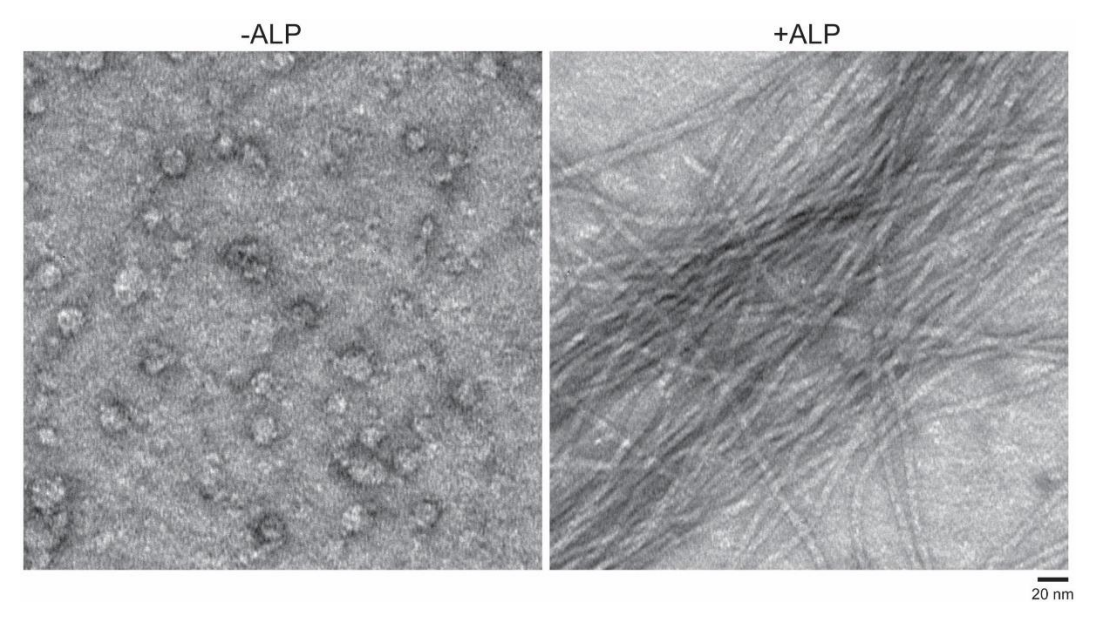


**Figure S1.** TEM images of nanostructures formed before and after adding ALP (2 U/mL) to the solution of 1P-KMe $_3$  (200  $\mu$ M, scale bar = 20 nm) for 24 h.

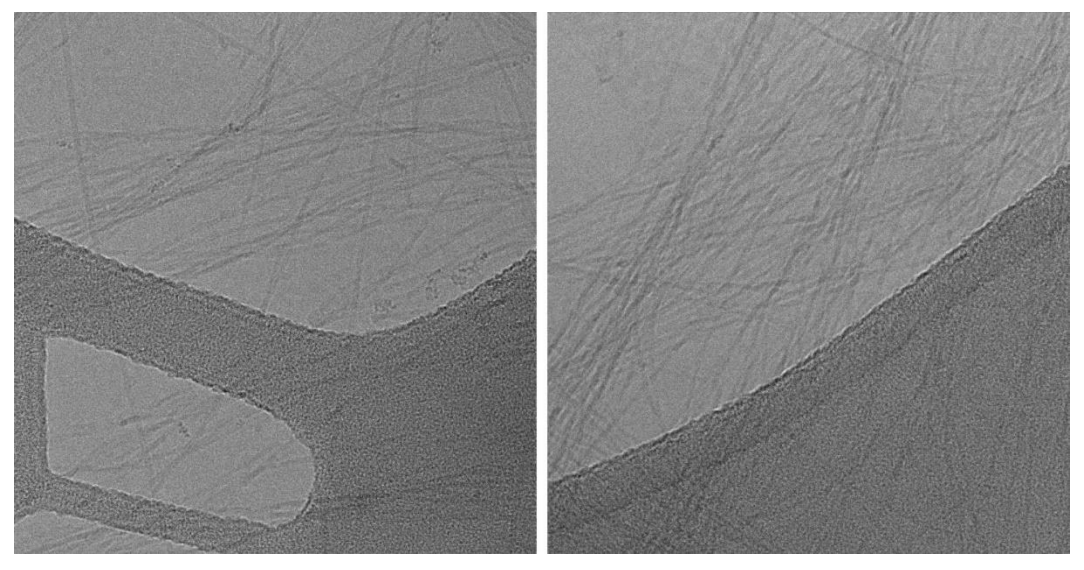


**Figure S2**. Representative cryo-EM images of nanostructures formed after adding ALP (2 U/mL) to the solution of 1P-KMe $_3$  (200  $\mu$ M). Scale bar is

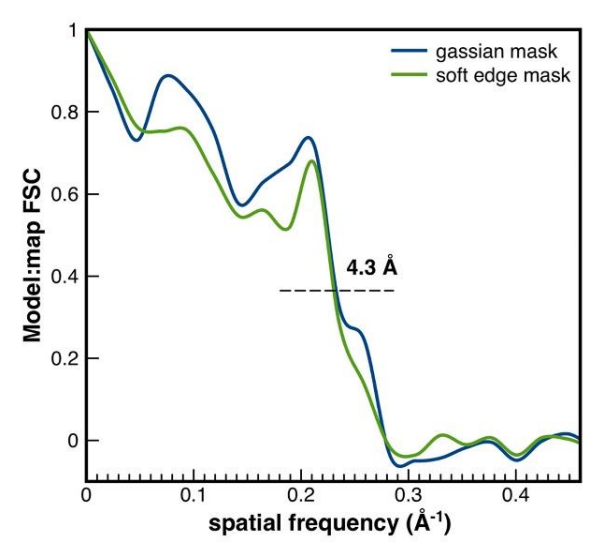


Figure S3. Fourier Shell Correlation (FSC) calculations

The model:map FSC calculation using a 0.38 criterion with two different masks, estimates the final reconstruction map to have a resolution of 4.3  $\hbox{\AA}.$ 

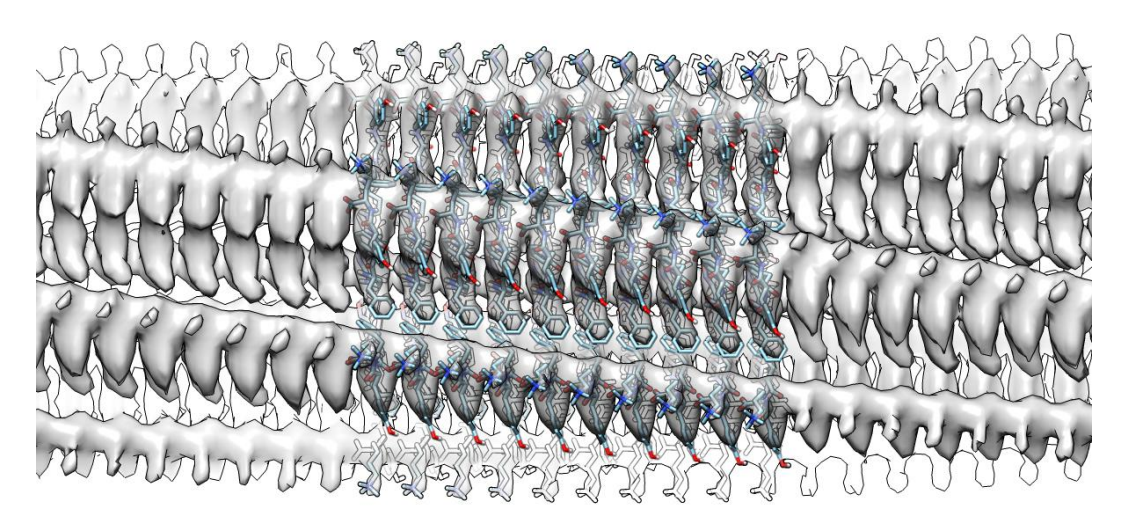
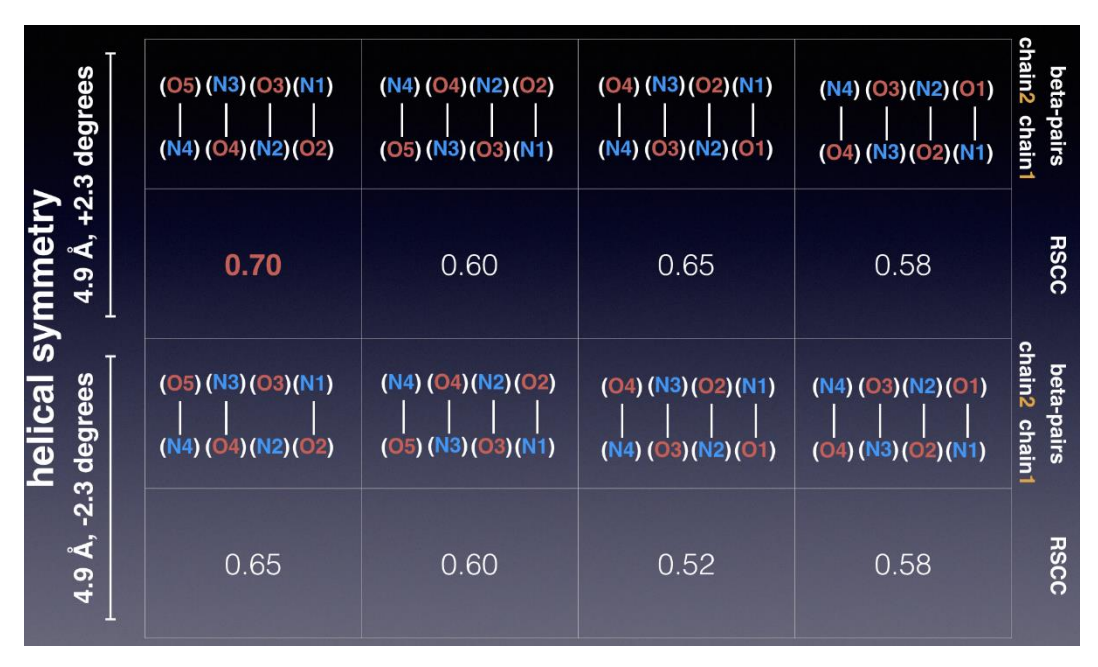
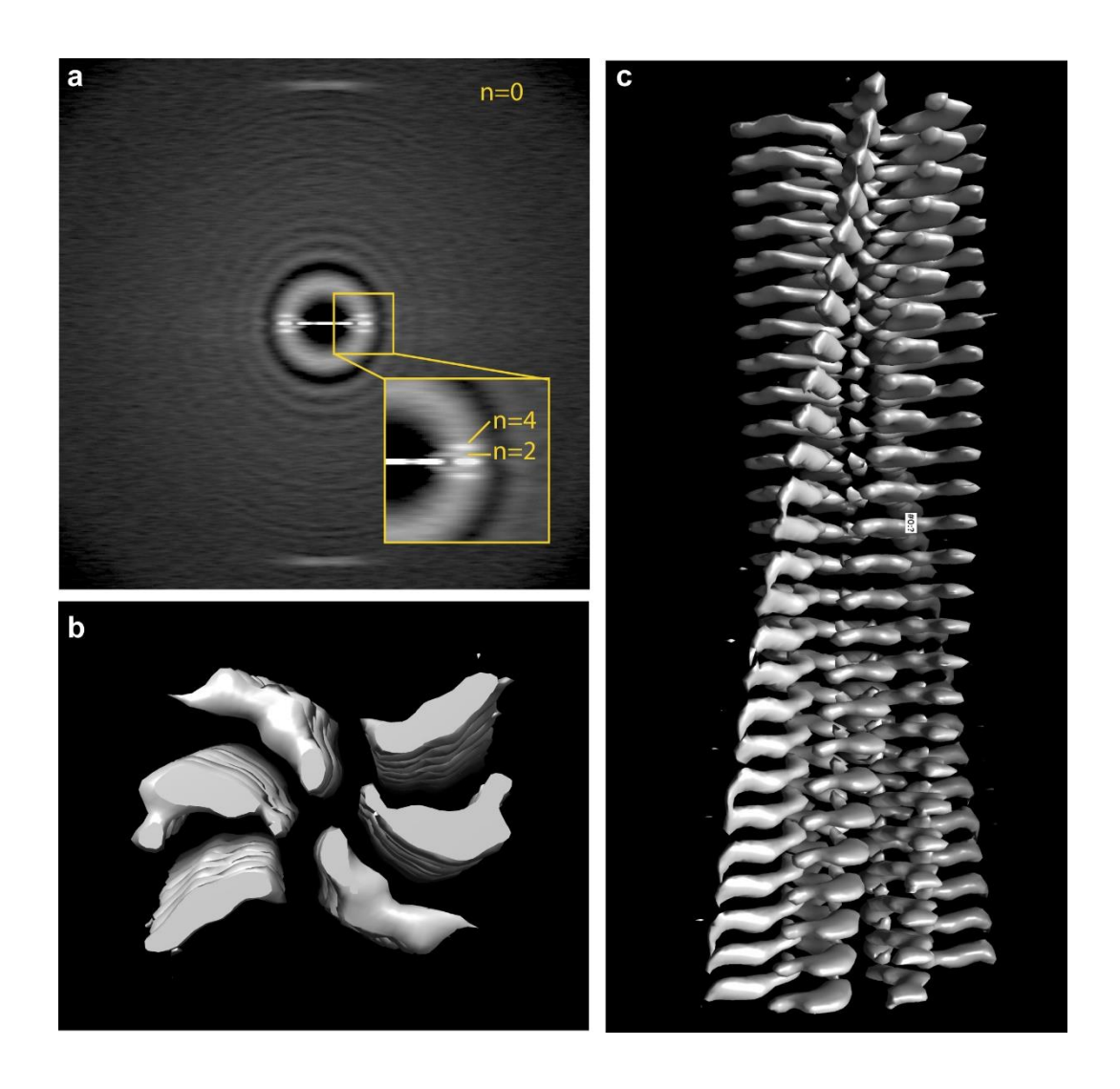


Figure S4. Side view of cryo-EM reconstruction of the 1-KMe<sub>3</sub> filaments.



**Figure S5.** The model:map real-space correlation coefficient (RSCC) of different PHENIX refinements. Due to the ambiguity of volume hand and hydrogen bonds between cross- $\beta$  layers, all possibilities were examined and their RSCC were listed in this figure.



**Figure S6.** a, Average power spectra of type 2 1-KMe $_3$  filaments. b,c, Top view (b) and side view (c) of 3D reconstruction of type 2 1-KMe $_3$  filaments from cryo-EM images.

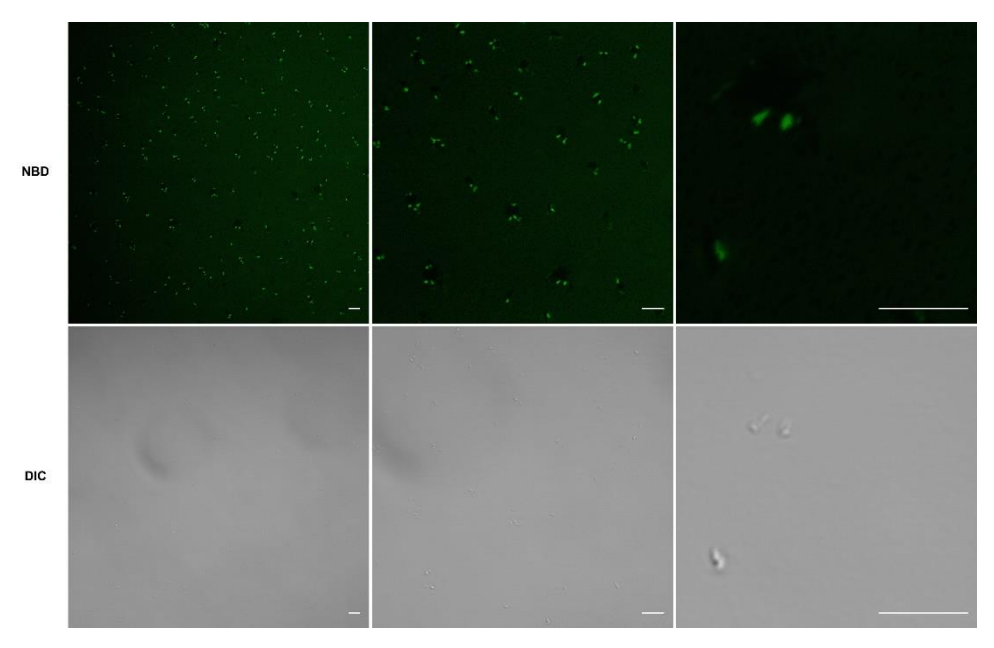
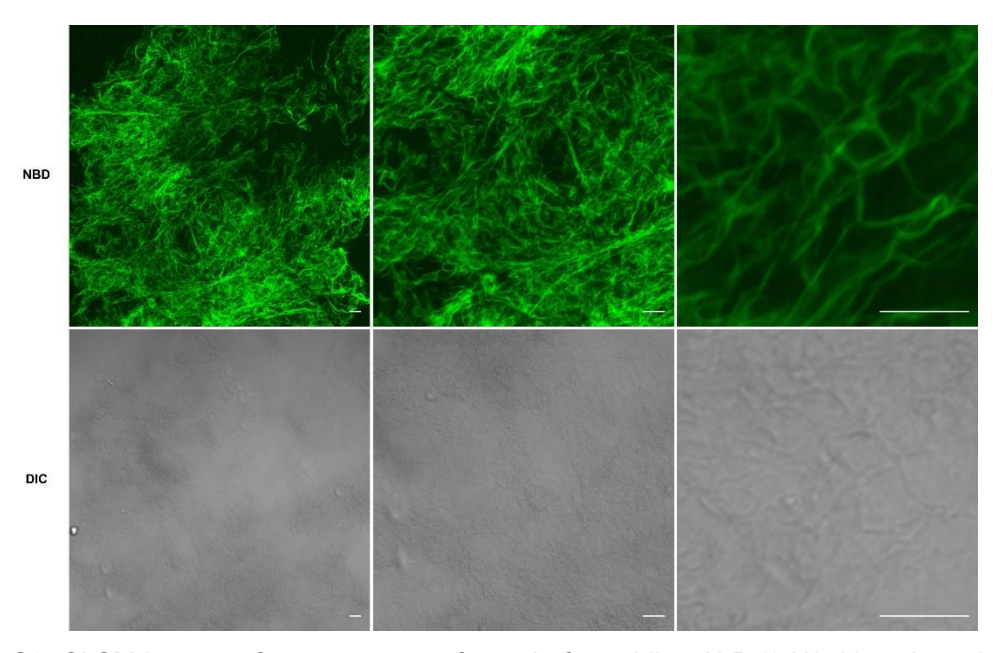


Figure S7. CLSM images of nanostructures formed by the solution of 1P-KMe3 (200  $\mu M).$  Scale bars, 5  $\mu m.$ 



**Figure S8.** CLSM images of nanostructures formed after adding ALP (2 U/mL) to the solution of 1P-KMe $_3$  (200  $\mu$ M) for 24 h. Scale bars, 5  $\mu$ m.

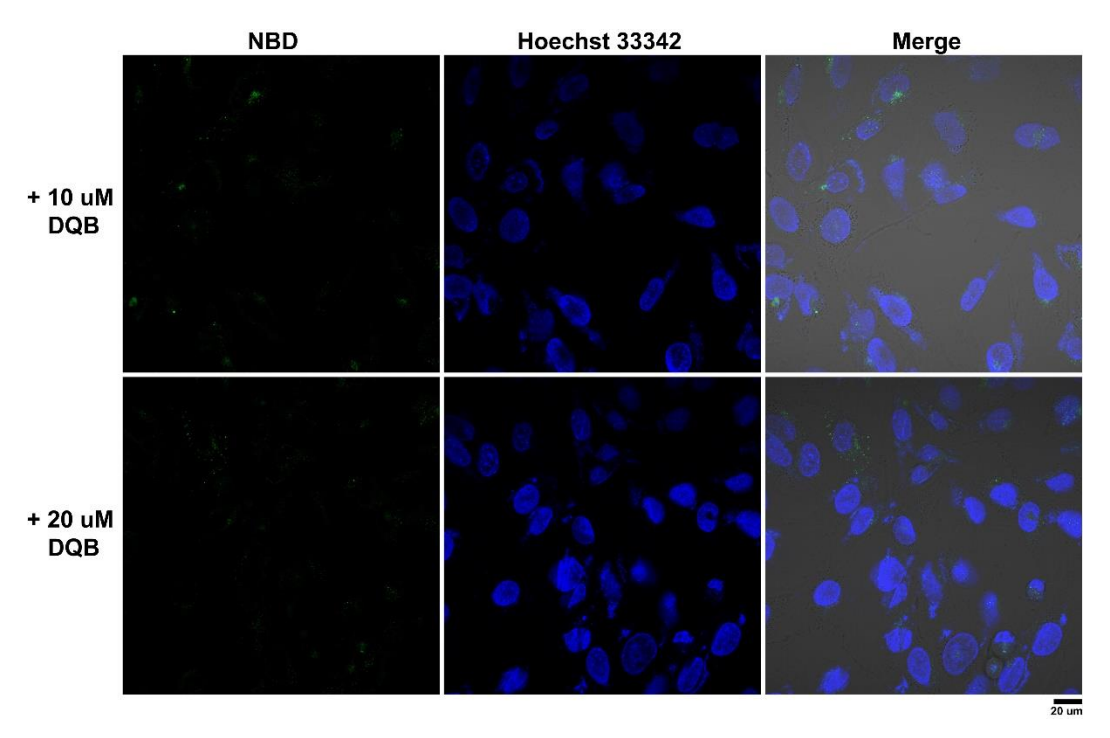


Figure S9. CLSM images of Saos-2 cells treated with 1P-KMe3 (200  $\mu$ M) and co-incubated with ALPL inhibitor (DQB) for 24 h. Scale bars, 20  $\mu$ M

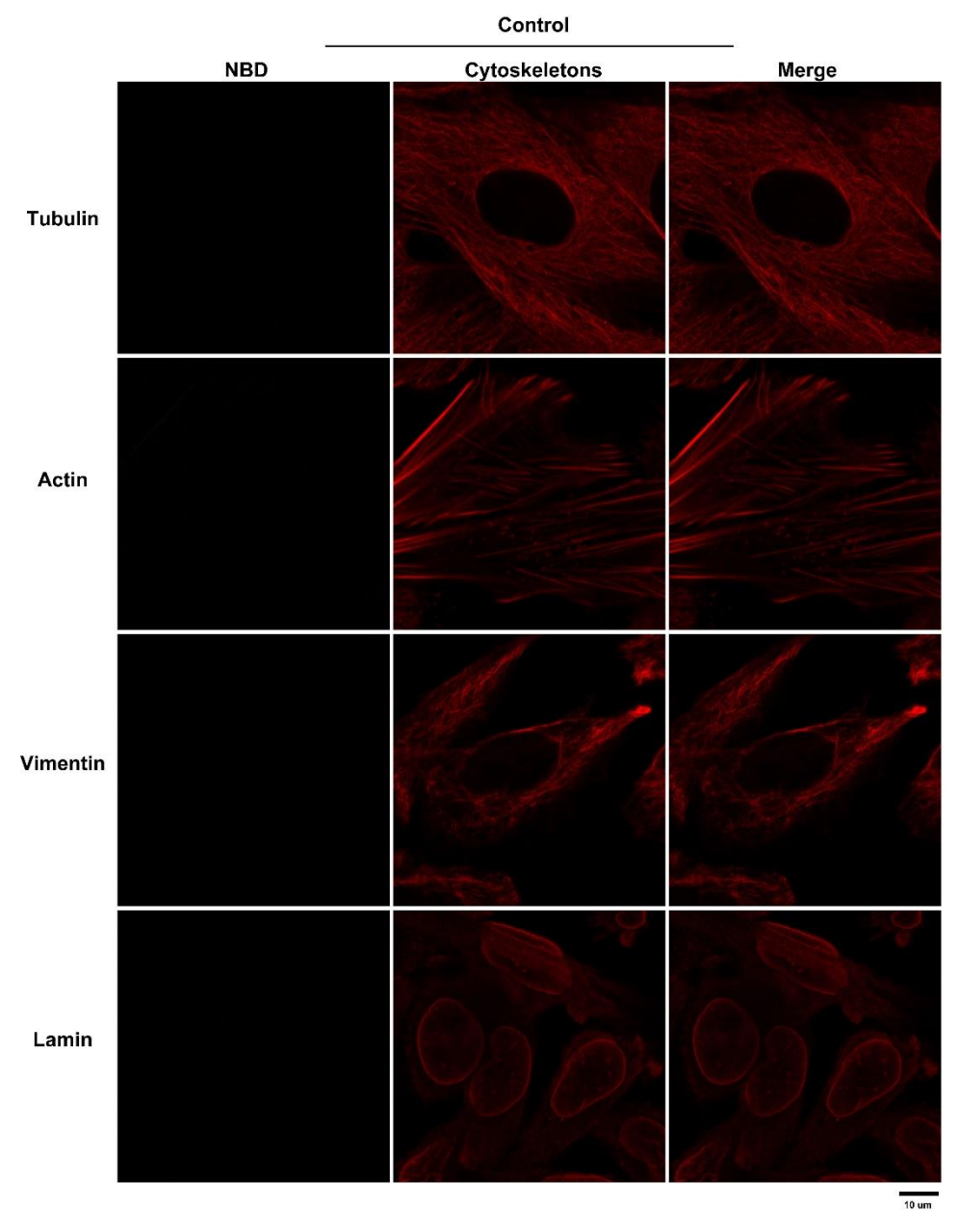
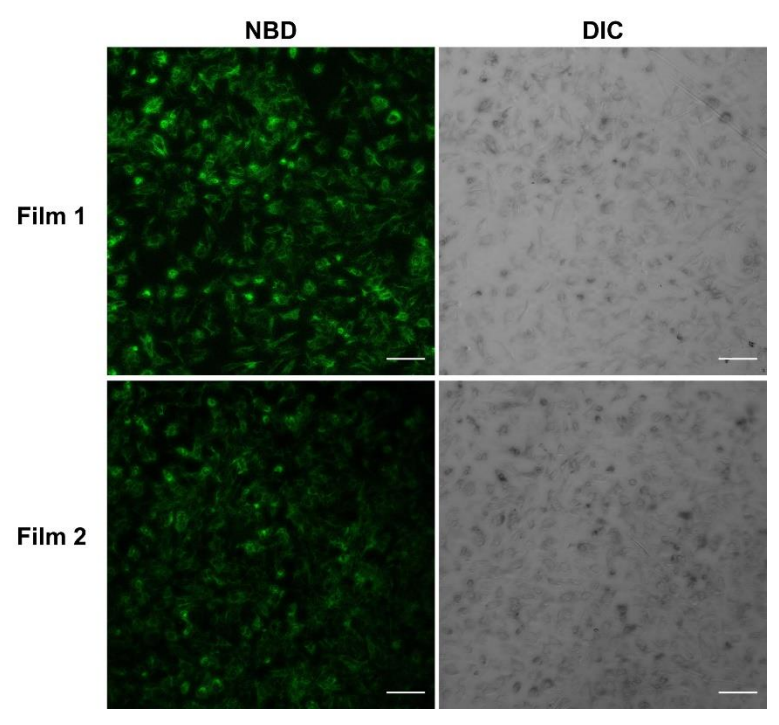
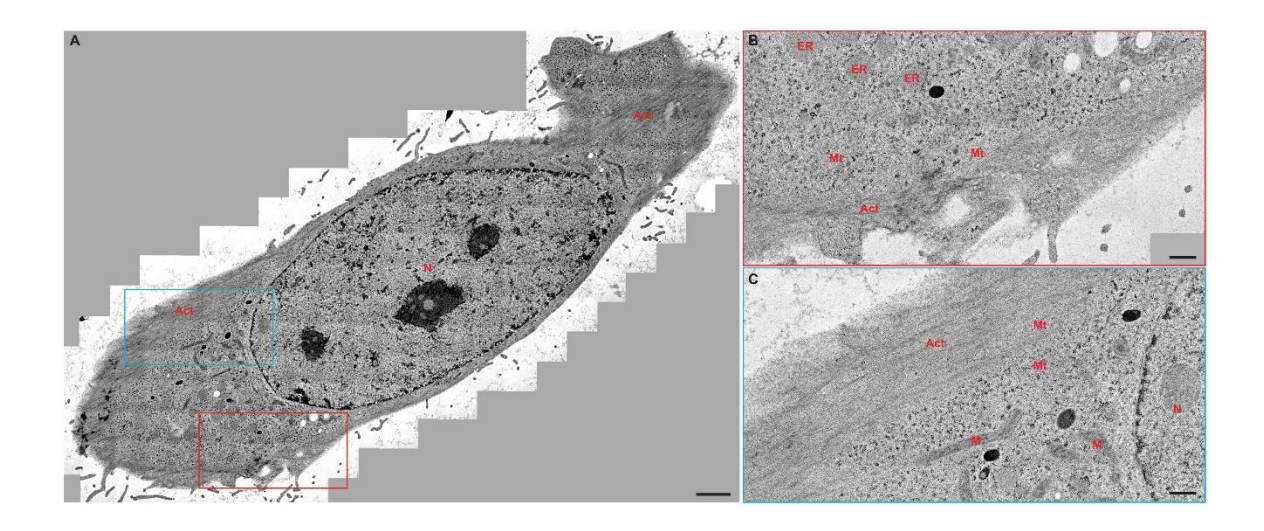


Figure S10. Immunofluorescent images (antibody staining for cytoskeleton proteins (red)) of the Saos-2 cells incubated with culture medium for 24 h. Scale bars, 10  $\mu$ m



**Figure S11.** Low magnification DIC and CLSM images of treated Saos-2 cells (1P-KMe<sub>3</sub> 200 μM, 24h) growing on Aclar plastic disks, right before high pressure freezing. Scale bars, 100 μm.



**Figure S12.** A, TEM image of a whole Saos-2 cell (wild-type, untreated) and higher magnification electron micrographs of the (B) red boxed area and the (C) blue boxed area. N: nucleus; M: mitochondria; Act: actin; Mt: microtubules; ER: endoplasmic reticulum. Scale bars in A, 2000 nm; B, C 500 nm.

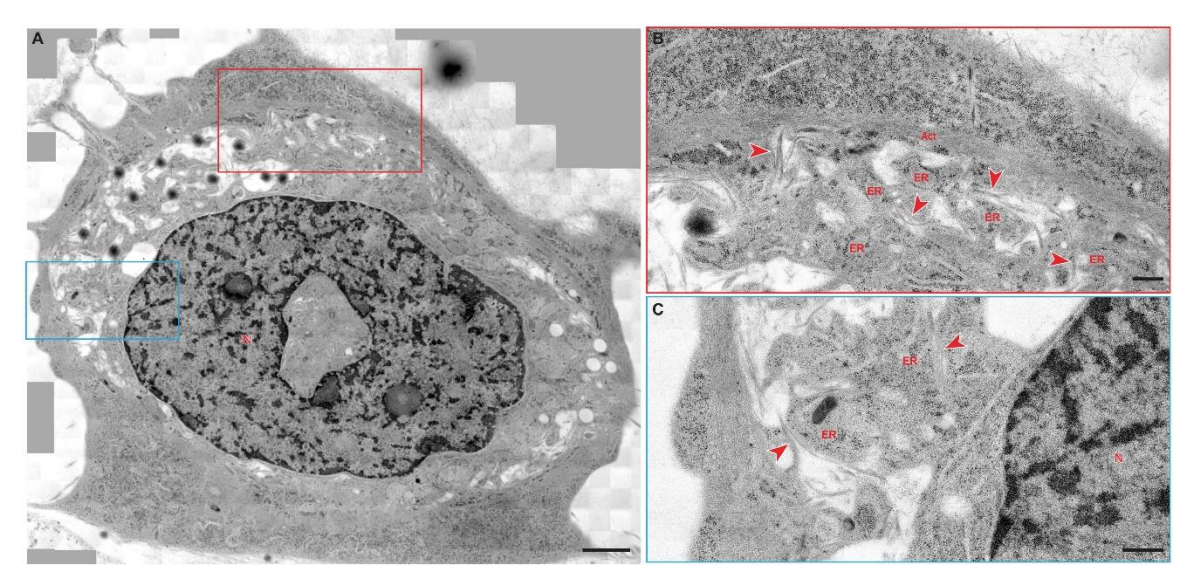


**Figure S13.** A, TEM image of a treated Saos-2 cell (1P-KMe $_3$  200  $\mu$ M, 24h) and higher magnification electron micrographs of the (B) red boxed area and the (C) blue boxed area showing artificial filaments inside the cells in the proximity of the endoplasmic reticulum. Solid red arrowheads indicate bundles of artificial filament; N: nucleus; Act: actin; ER: endoplasmic reticulum. Scale bars in A, 2000 nm; B, C 500 nm.

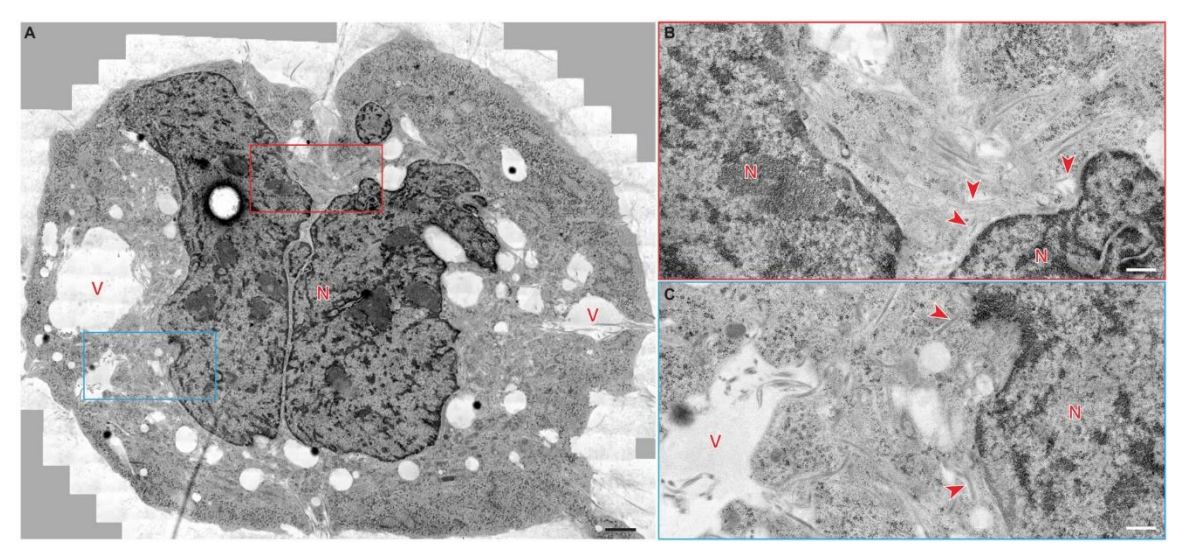


**Figure S14.** A, TEM image of a treated Saos-2 cell (1P-KMe $_3$  200  $\mu$ M, 24h) and higher magnification electron micrographs of the (B) red boxed area and the (C) blue boxed area showing artificial filaments inside the cells close to the nucleus. Solid red arrowheads indicate bundles of artificial filament; N: nucleus; V: vacuoles. Scale bars in A, 2000 nm; B, C 500 nm.

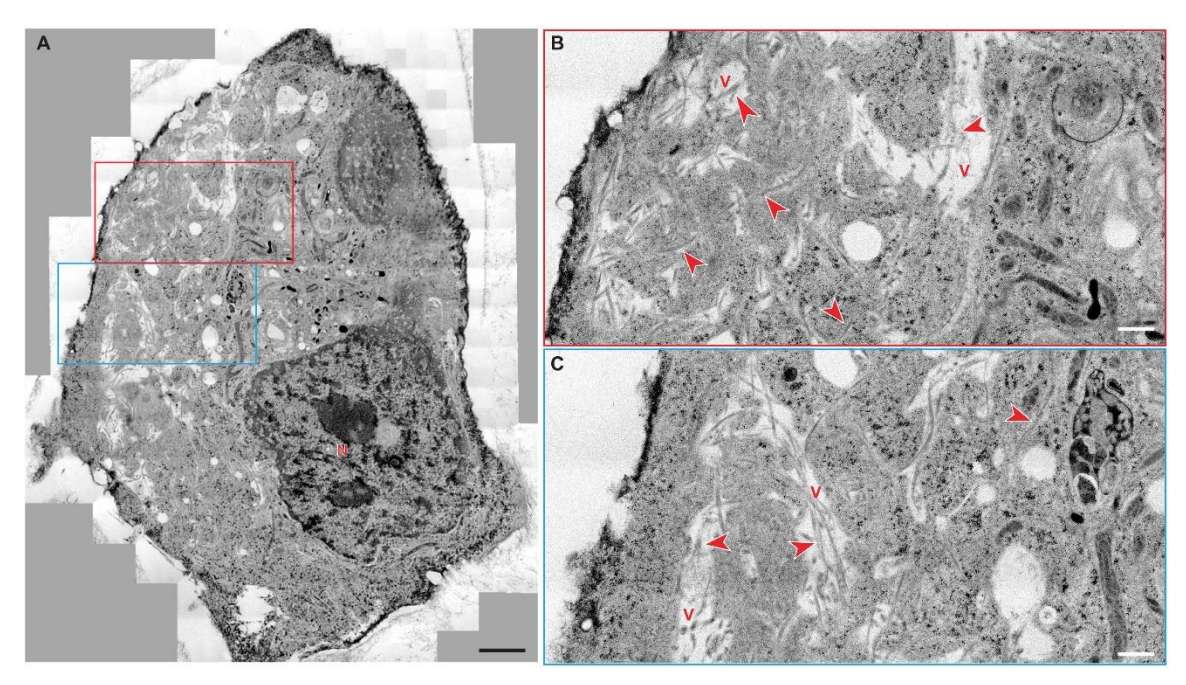


**Figure S15.** A, TEM image of a treated Saos-2 cell (1P-KMe $_3$  200  $\mu$ M, 24h) and higher magnification electron micrographs of the (B) red boxed area and the (C) blue boxed area showing artificial filaments in the cytosol and inside vacuoles. Solid red arrowheads indicate bundles of artificial filament; N: nucleus; V: vacuoles. Scale bars in A, 2000 nm; B, C 500 nm.

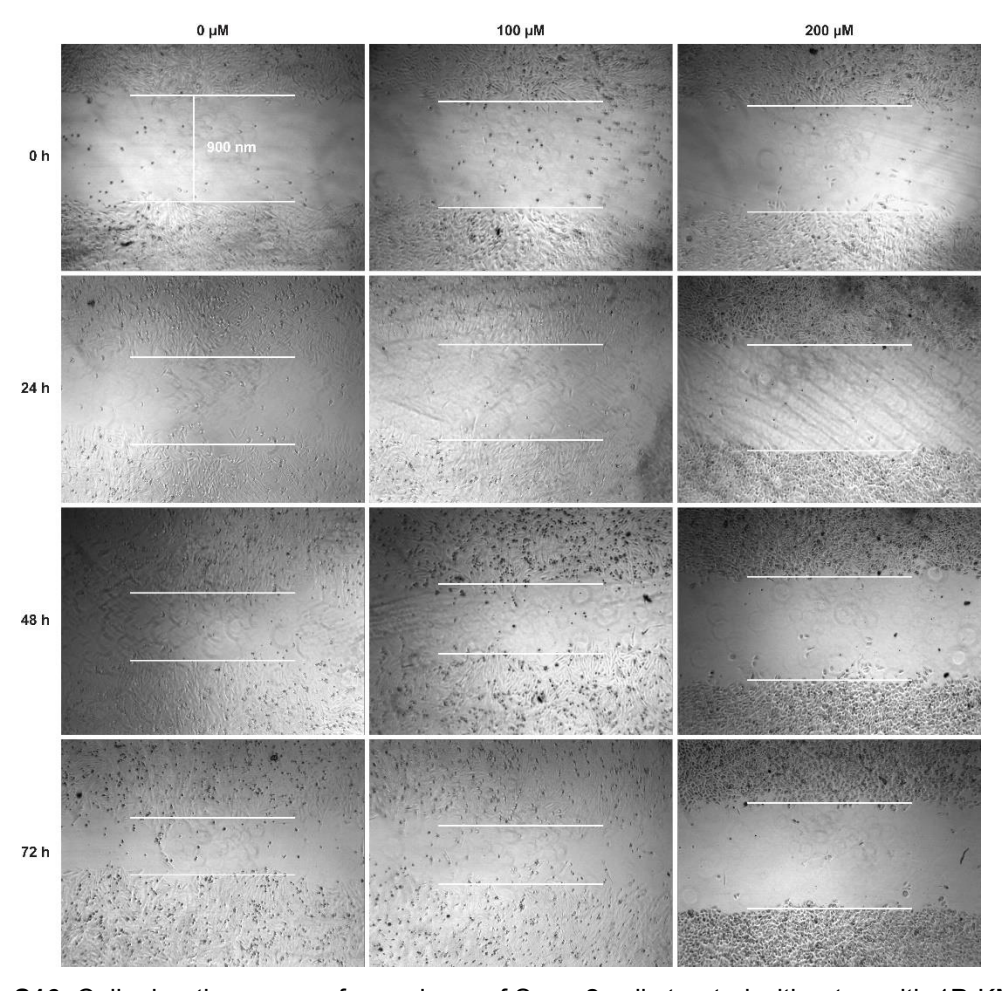


**Figure S16.** Cell migration assay of monolayer of Saos-2 cells treated without or with 1P-KMe $_3$  (100 or 200  $\mu$ M) at different time points.

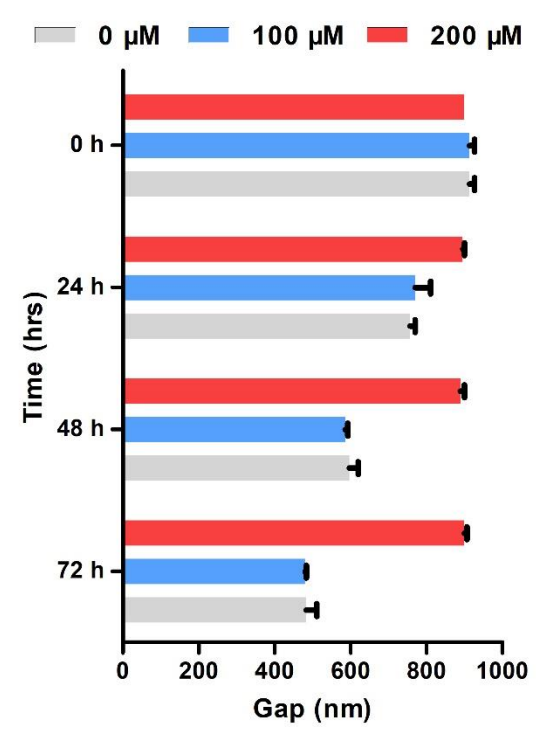


**Figure S17.** Measurement of cell migration assay of monolayer of Saos-2 cells treated without or with 1P-KMe $_3$  (100 or 200  $\mu$ M) at different time points.

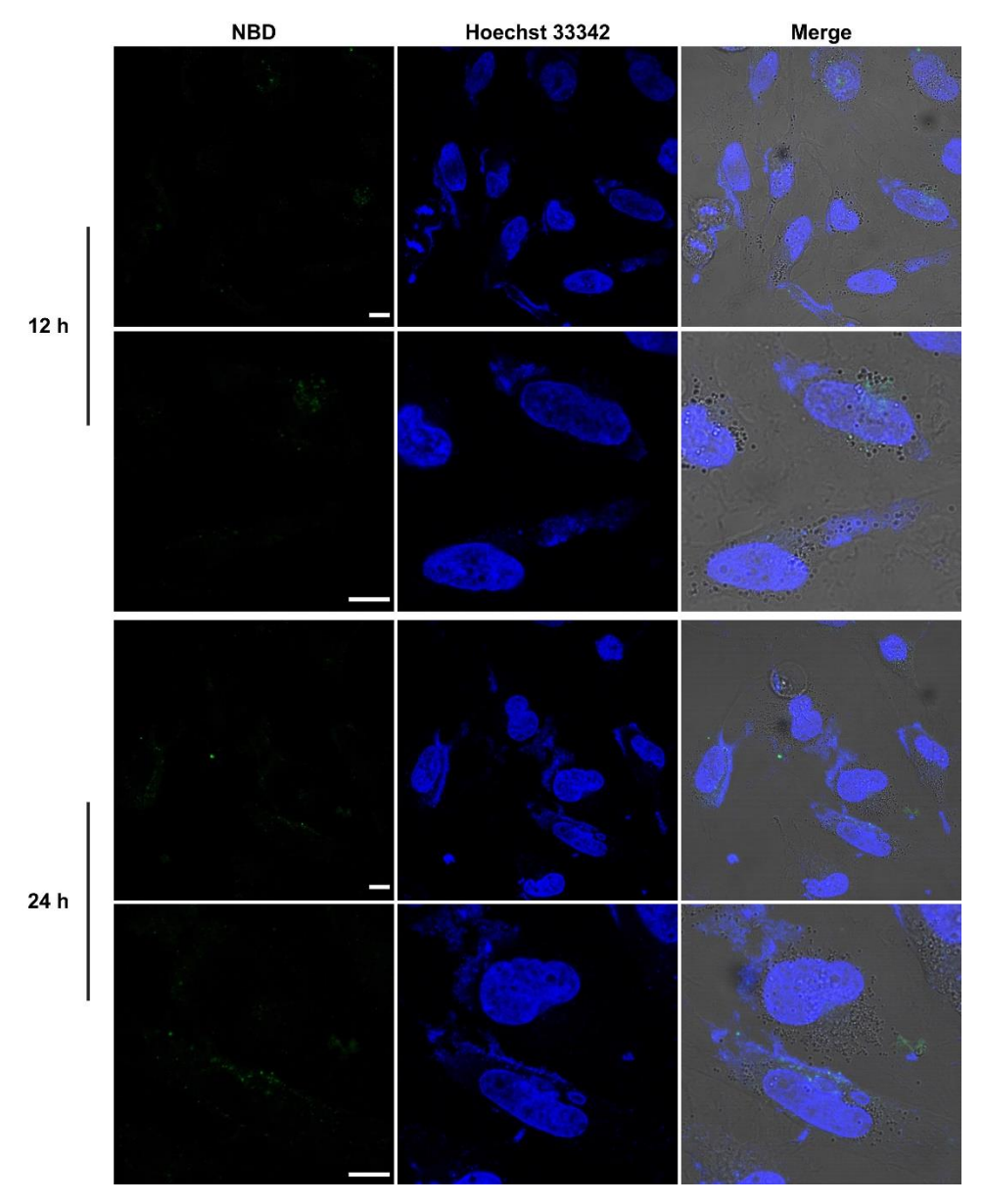


**Figure S18.** CLSM images of Saos-2 cells treated with 1P-KMe $_3$  (100  $\mu$ M) for 12 or 24 h. Scale bars, 10  $\mu$ m.

Scheme S1 Molecular structures of 2P-KMe<sub>3</sub>, 3P-KMe<sub>3</sub> and 1P-K.

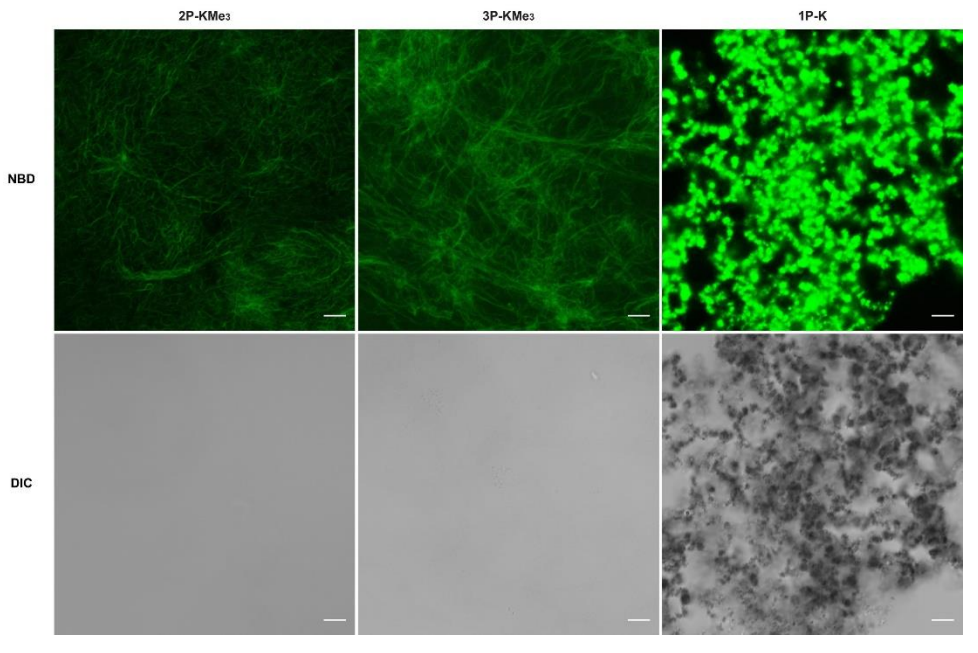


**Figure S19.** CLSM images of nanostructures formed after adding ALP (2 U/mL) to the solution of 2P-KMe $_3$ , 3P-KMe $_3$  and 1P-K (200  $\mu$ M) for 24 h. Scale bars, 5  $\mu$ m.

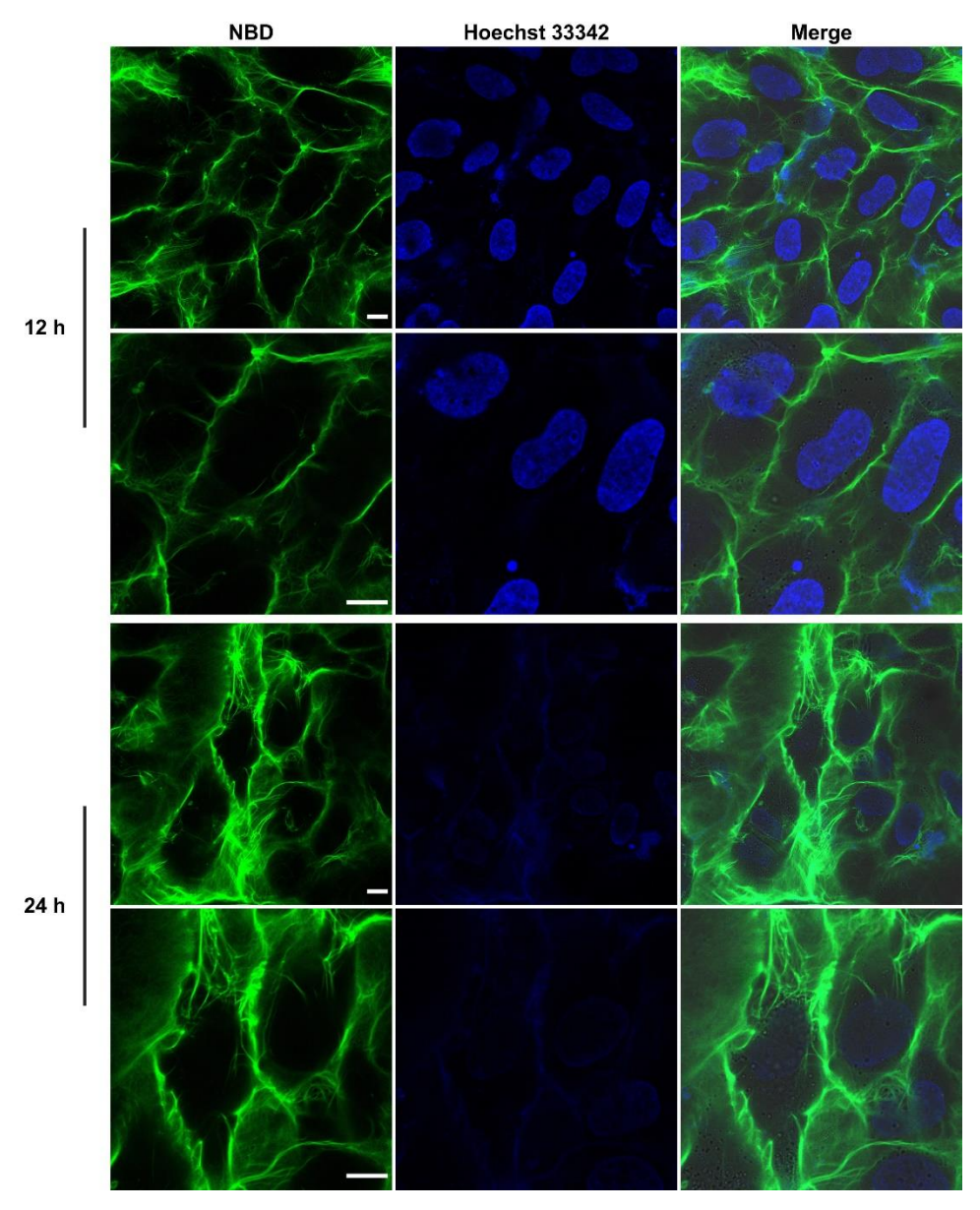


**Figure S20.** CLSM images of Saos-2 cells treated with 2P-KMe $_3$  (200  $\mu$ M) for 12 or 24 h. Scale bars, 10  $\mu$ m.

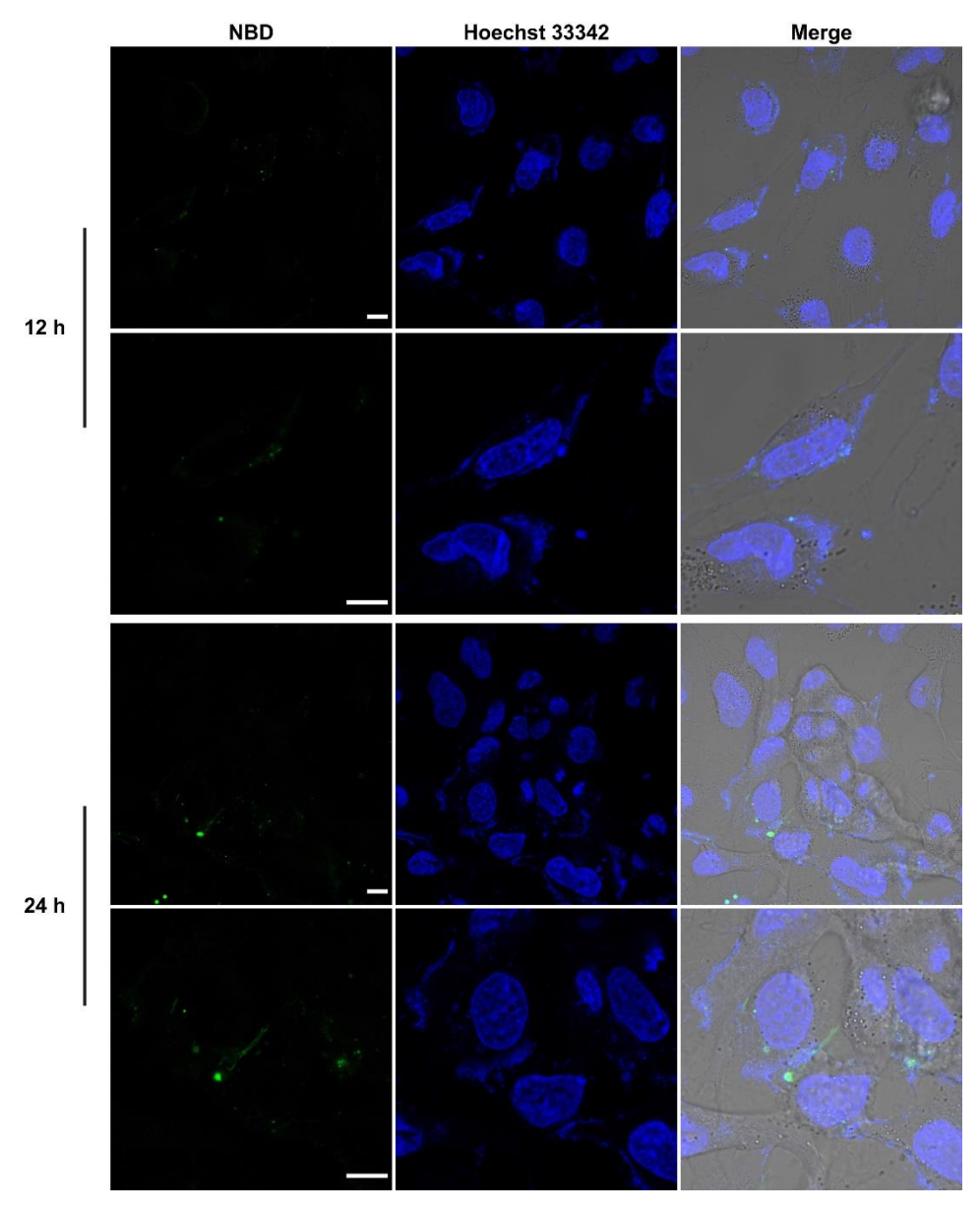


**Figure S21.** CLSM images of Saos-2 cells treated with 3P-KMe $_3$  (200  $\mu$ M) for 12 or 24 h. Scale bars, 10  $\mu$ m.

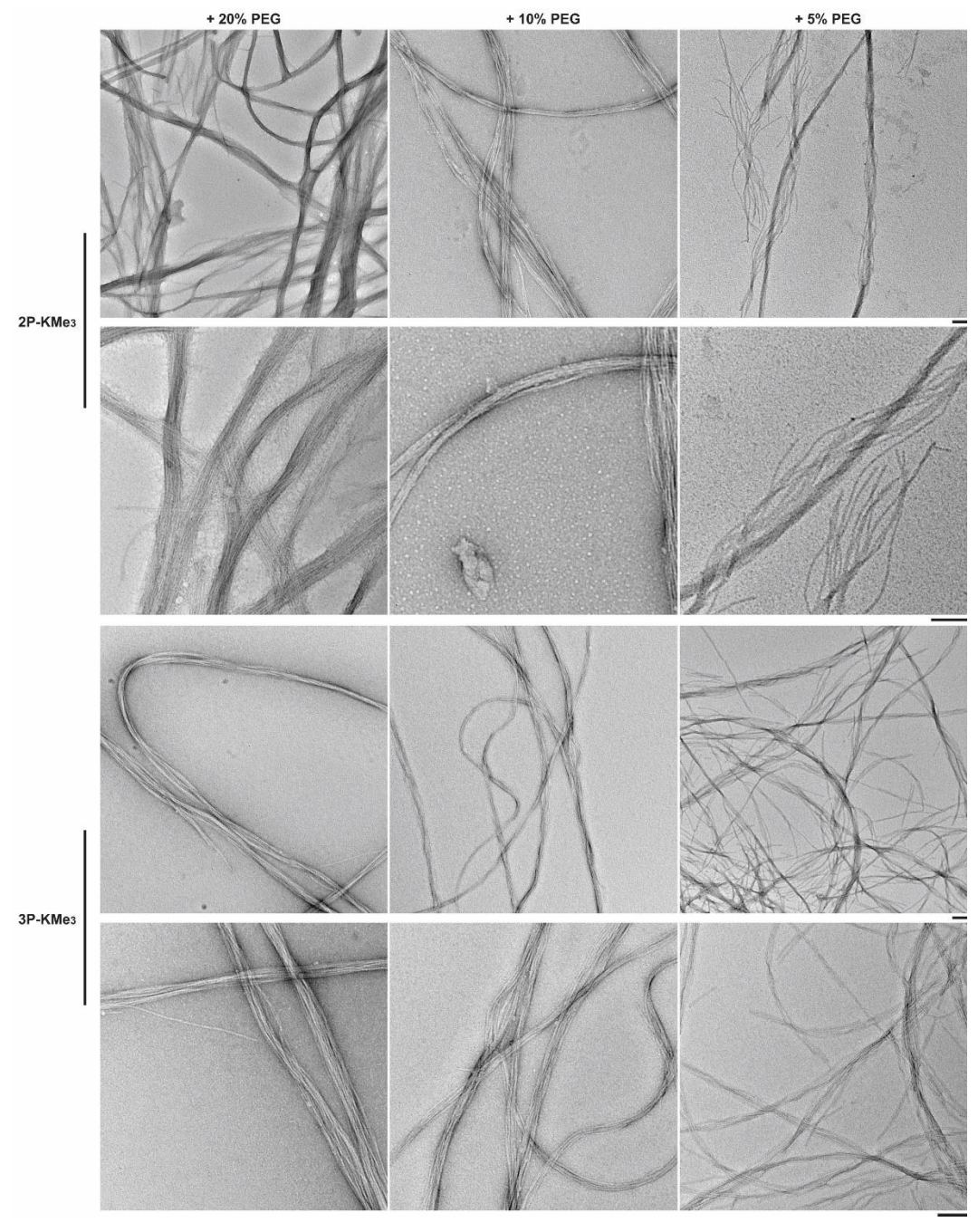


**Figure S22.** TEM image of nanostructures formed after adding ALP (2 U/mL) to the solution of 2P-KMe $_3$  or 3P-KMe $_3$  (200  $\mu$ M) for 24 h, in the presence of 5 %, 10 %, and 20 % (w/v) PEG 20000. Scale barS = 100 nm.

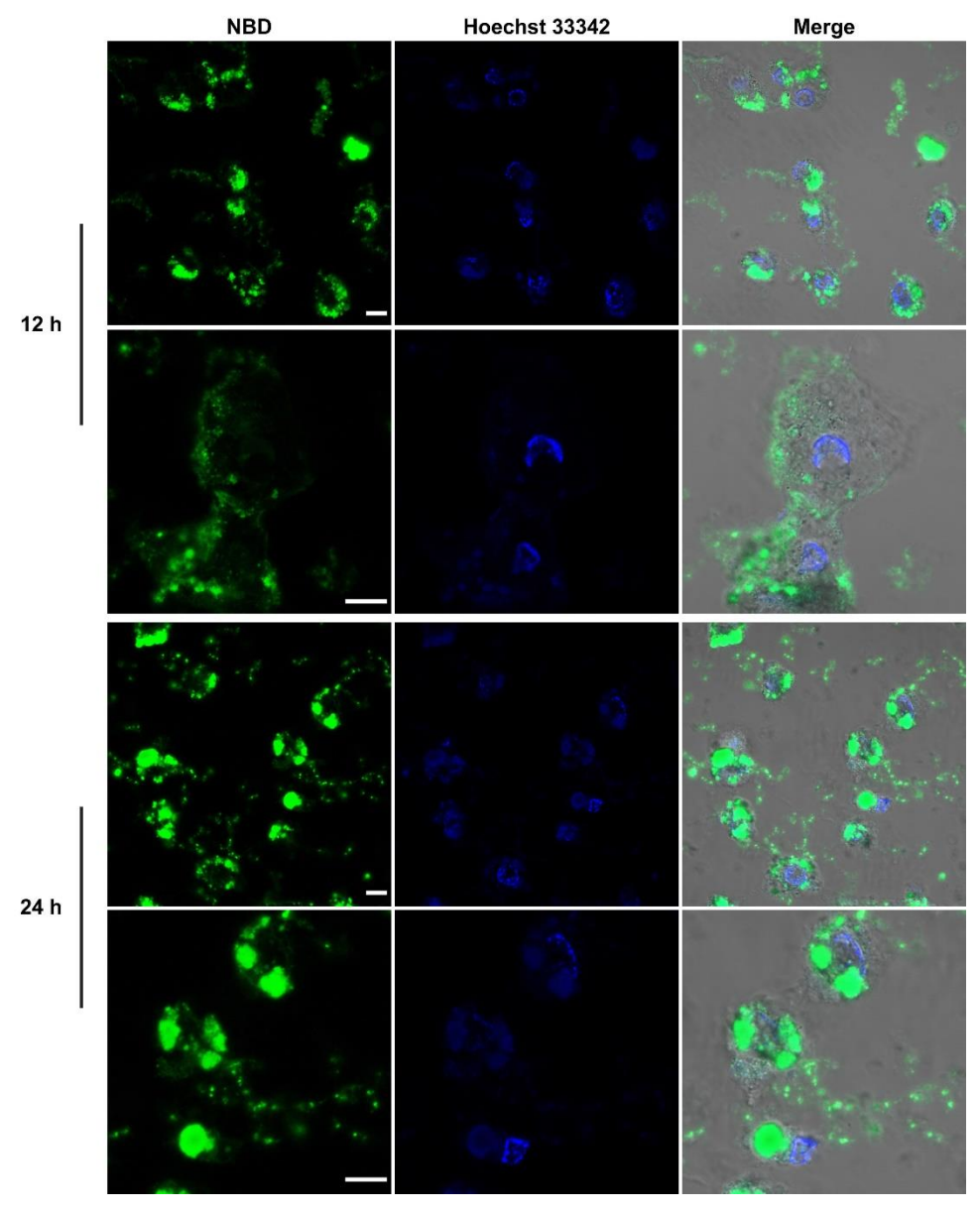


**Figure S23.** CLSM images of Saos-2 cells treated with 1P-K (200  $\mu M)$  for 12 or 24 h. Scale bars, 10  $\mu m.$ 

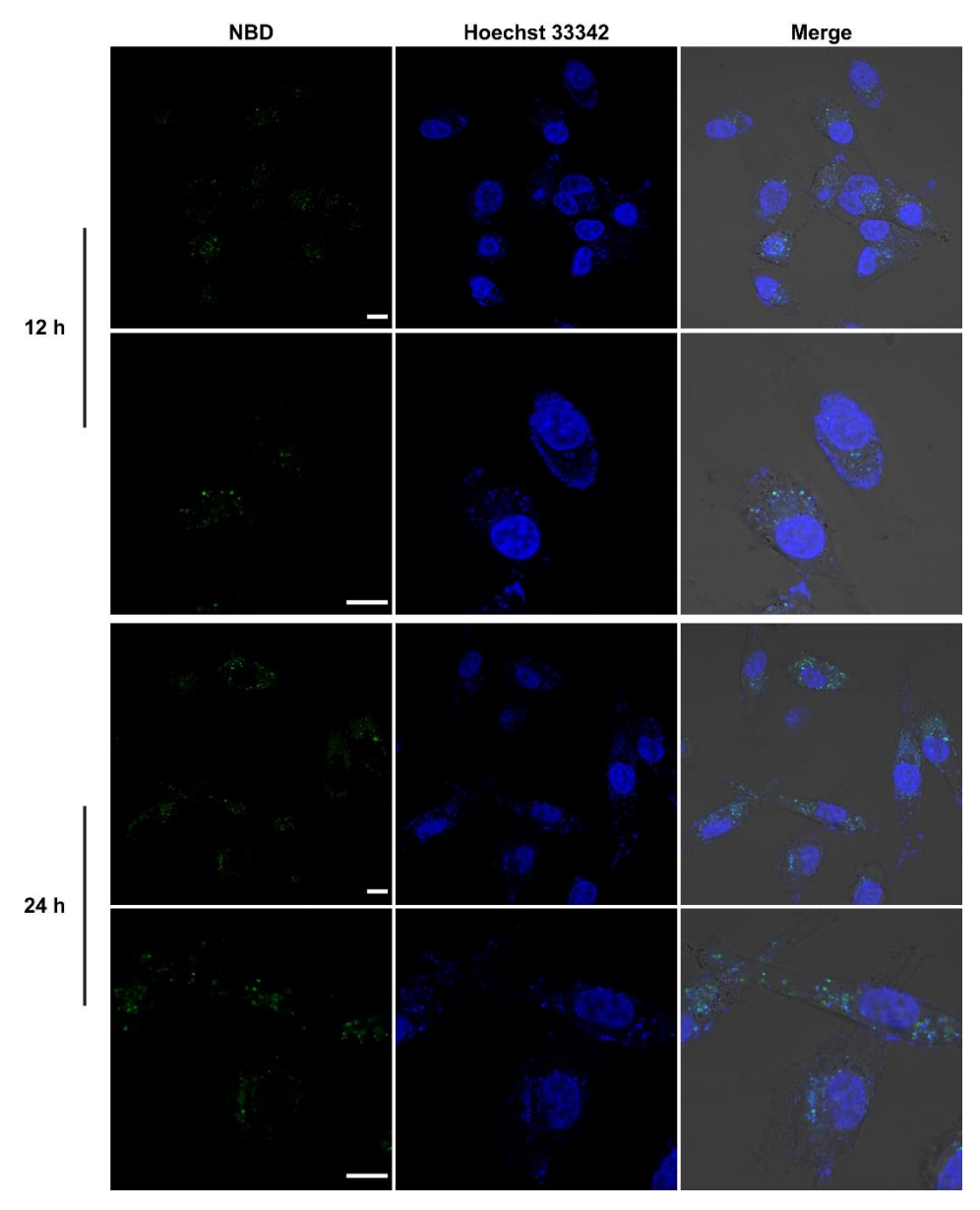


Figure S24. CLSM images of HS-5 cells treated with 1P-KMe $_3$  (200  $\mu$ M) for 12 or 24 h. Scale bars, 10  $\mu$ m.

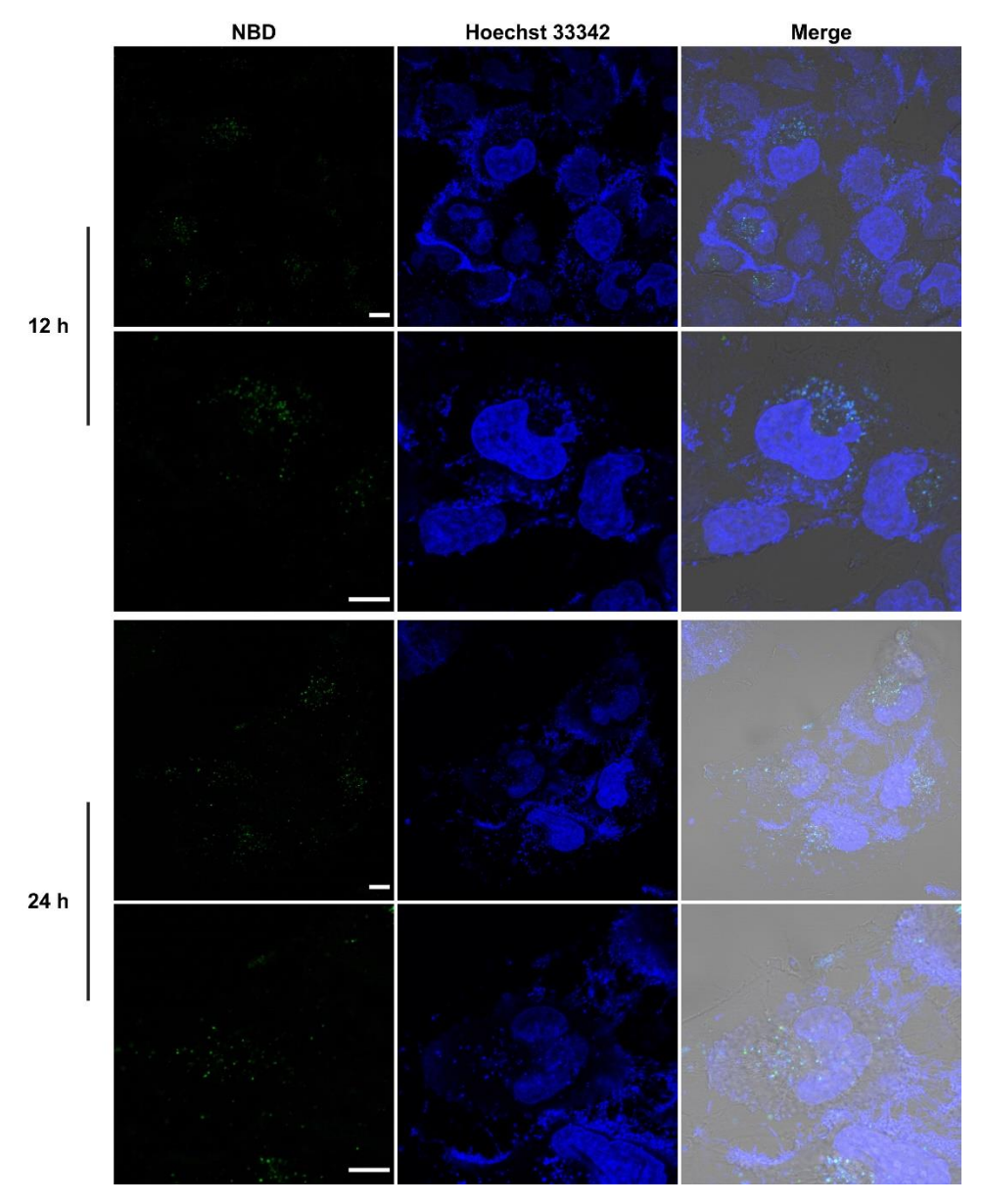
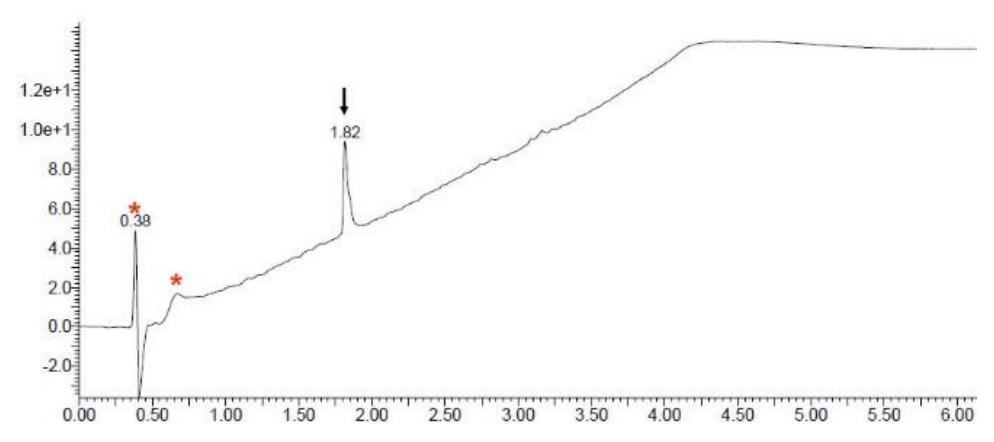
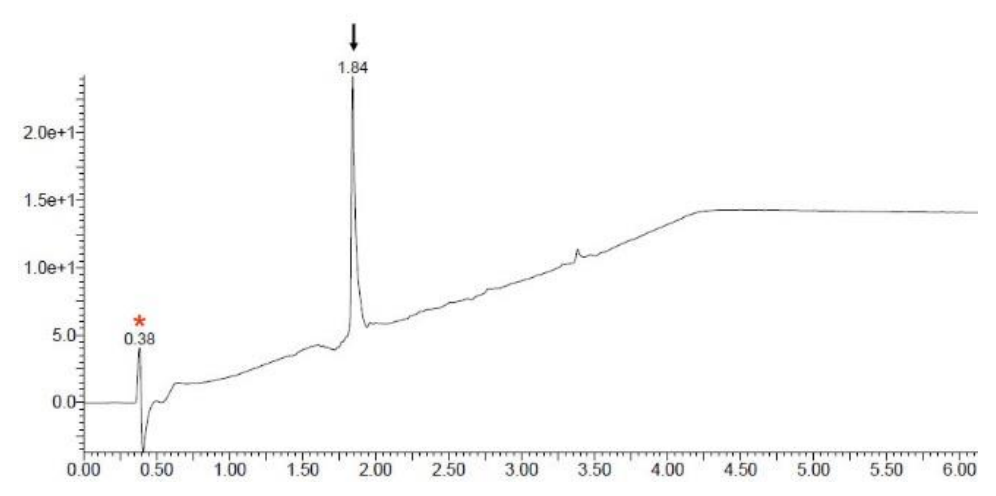


Figure S25. CLSM images of T98G cells treated with 1P-KMe3 (200  $\mu M)$  for 12 or 24 h. Scale bars, 10  $\mu m.$ 



**Figure S26.** LC spectra of 1P-KMe<sub>3</sub>. Asterisk indicates the systematic peaks, and arrow indicates the product.



 $\textbf{Figure S27.} \ \, \text{LC spectra of 2P-KMe}_{3}. \ \, \text{Asterisk indicates the systematic peaks, and arrow indicates the product.}$ 

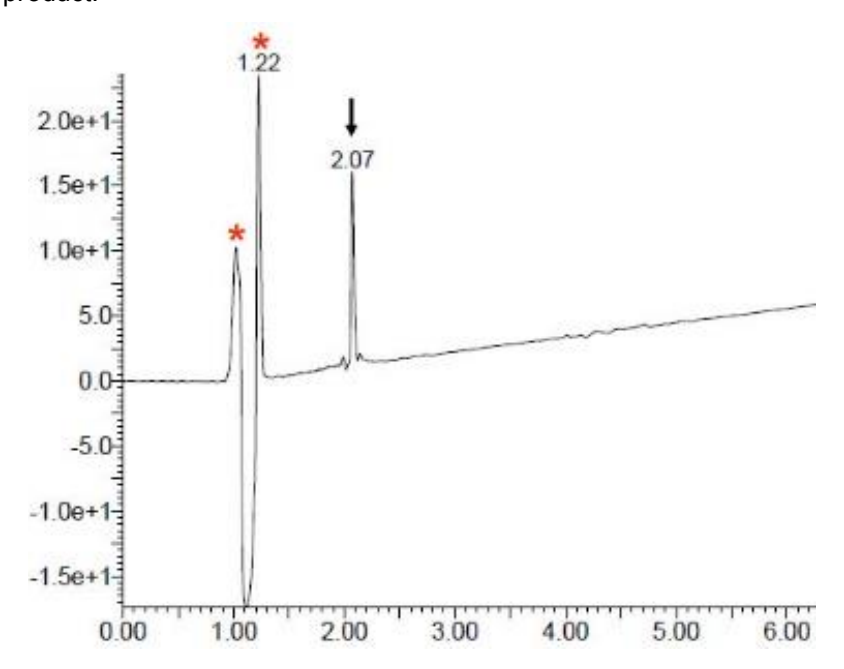


**Figure S28**. LC spectra of 3P-KMe<sub>3</sub>. Asterisk indicates the systematic peaks, and arrow indicates the product.

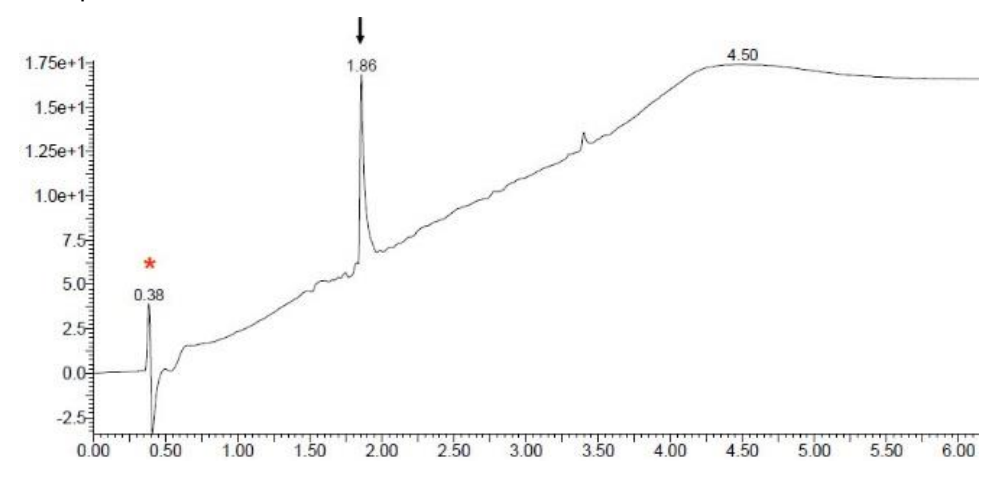


**Figure S29**. LC spectra of 1P-K. Asterisk indicates the systematic peaks, and arrow indicates the product.

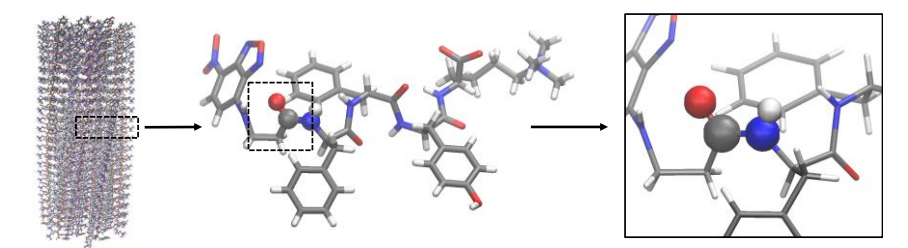


**Figure S30.** The *cis* configuration of the first peptide bond that connects NBD with Phe in the EM structural model.

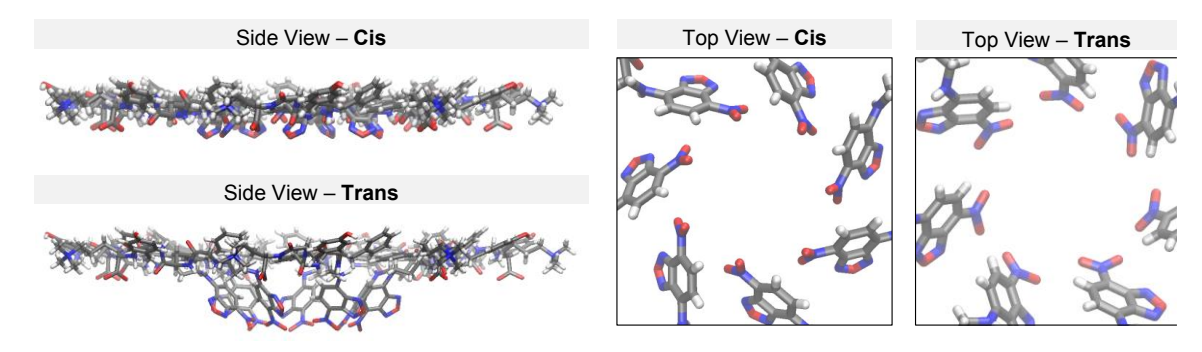


**Figure S31.** The structural difference between the *cis* and *trans* filament models.

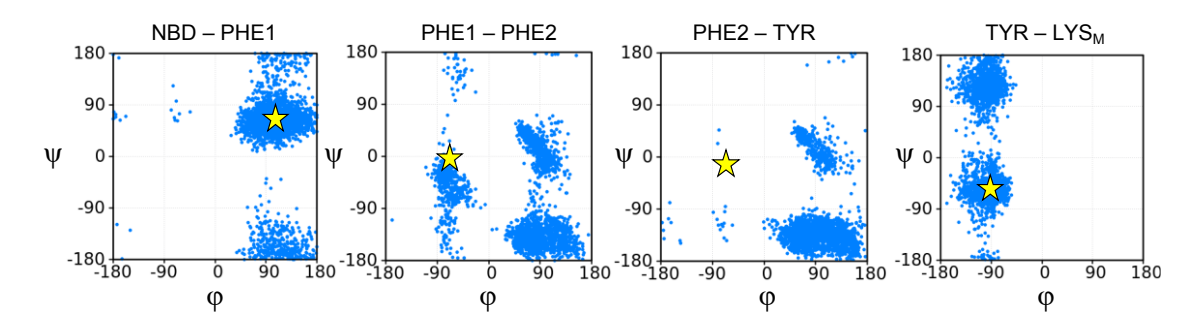


**Figure S32.** Ramachandran plots of the four peptide bonds for the *trans* peptide in solution from four independent explicit solvent simulations up to 250 ns of sampling. The initial dihedral angles of peptide bonds obtained from the EM structure are marked as yellow star.

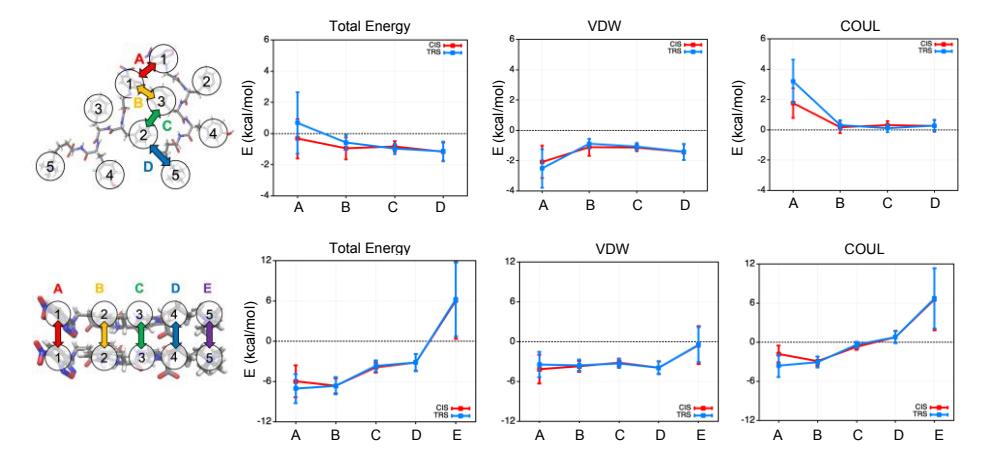


**Figure S33.** Pairwise interaction energies between neighboring residues for (top) peptide pairs in the same layer and (bottom) peptide pairs in the adjacent layers. The pairs of interactions (labeled as A-D in the top panels and A-E in the bottom panels) are computed using 100 snapshots that contain 22 layers with 154 lateral and perpendicular pairs each and compared for the *cis* and *trans* fiber models when their structures remain close to the EM structural model; for each case, the total interaction energy is further decomposed into van der Waals (VDW) and Coulombic (COUL) components, which are shown explicitly. Note that a distance-dependent dielectric model is used in the Coulombic component calculations for this analysis.

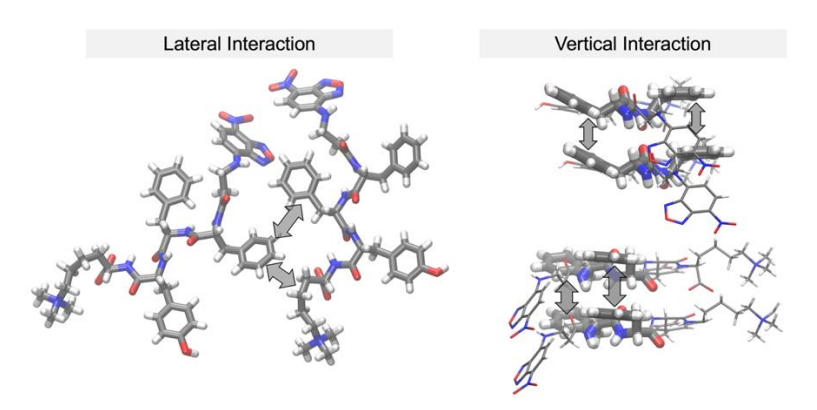


**Figure S34.** Van der Waals interactions (lateral) and  $\pi$ - $\pi$  stacking (vertical) form the dominant stabilizing factors that stabilize the filament structure, and hydrogen bonding interactions among peptide bonds also contribute to the stabilization of vertical pairs.

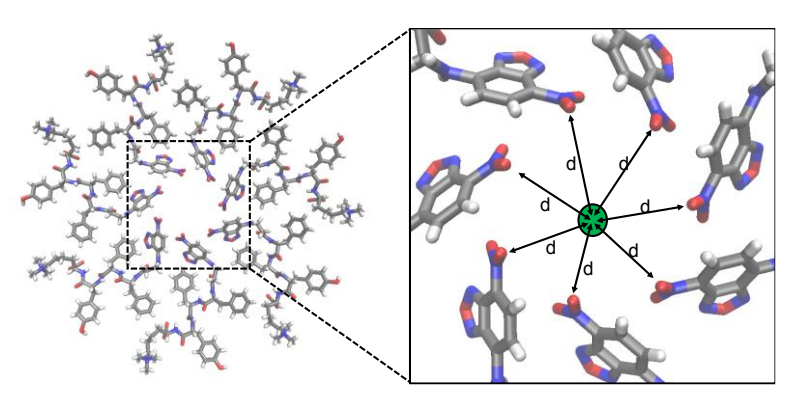


**Figure S35.** The minimal distance between a nitrogen atom of the nitro group in NBD and a solvent/ion is calculated to define whether the water or the ion is adsorbed.

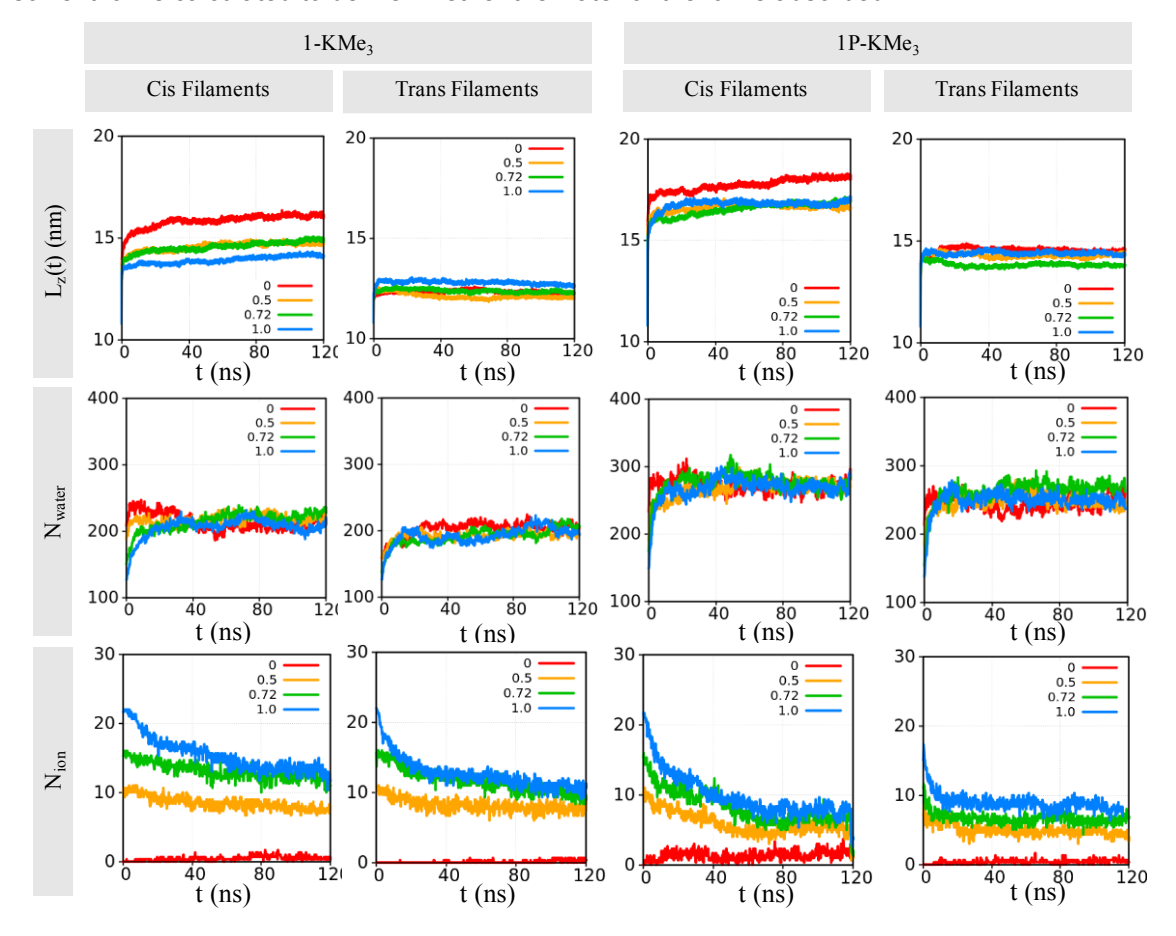


**Figure S36.** Length of the fiber  $(L_z)$  and the number of internal water/ions  $(N_{water}, N_{ion})$  during MD simulations for 1-KMe<sub>3</sub> and 1P-KMe<sub>3</sub> systems with different NBD-peptide conformation (cis/trans) and initial number of ions in the core of the filament  $(f_{ion})$ .

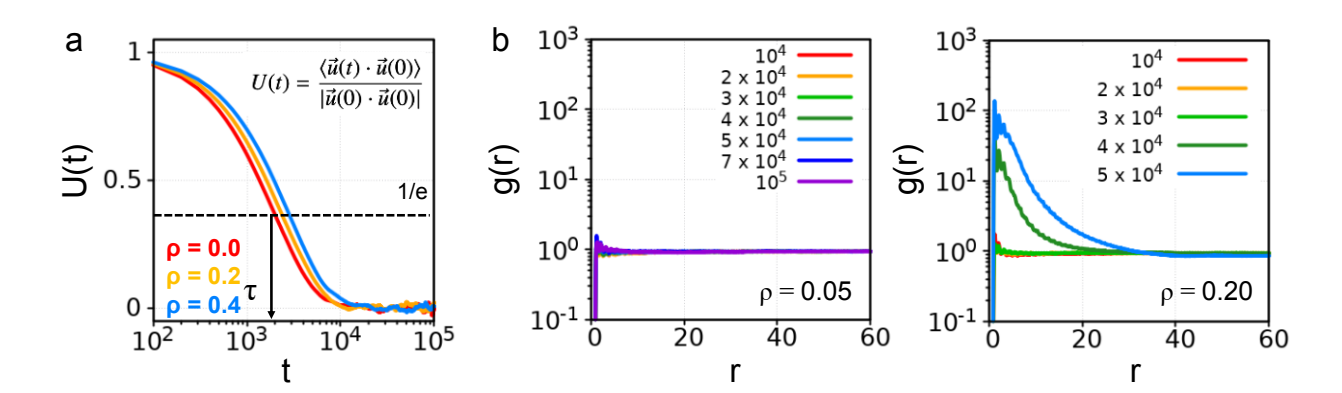


**Figure S37.** a, Auto correlation function of end to end vector U(t) of a single polymer in crowded media with different crowder volume fraction. b, Representative plots of the radial distribution function g(r) of monomers at different simulation times. The left panel corresponds to a case in which the polymers remain separated in solution, and the right panel corresponds to the case of polymer bundle formation.

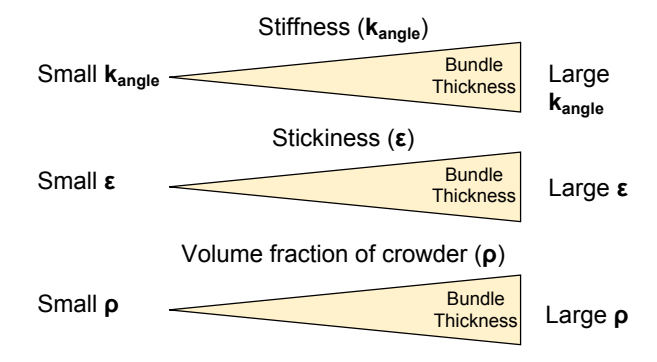


Figure S38. Three physical factors that affect bundling of polymer chains. The stiffness ( $k_{angle}$ ) of polymer chain, interaction strength between monomers ( $\epsilon$ ), and volume fraction of non-interacting crowders ( $\rho$ ) affect the bundling of the polymer chains.

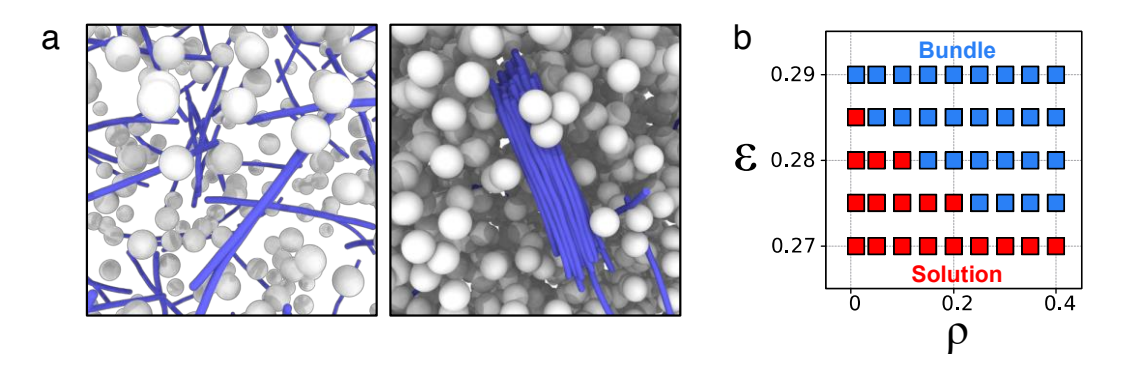


Figure S39. Coarse-grained simulations on the bundles of the filaments. a, Simulation snapshot of low (left) and high crowded media. b, Phase diagram with respect to stickiness ( $\epsilon$ ) and crowder volume fraction ( $\rho$ ). Blue and red square represent bundled and solution phases, respectively.

## **Supplemental Notes**

#### **Note S1. Cis and Trans Model Filaments**

To probe whether the *cis* and *trans* models feature significantly different inter-peptide interactions, we calculate the average interaction energies between neighboring peptides in lateral (i.e., in the same peptide layer) and perpendicular (i.e., between neighboring peptide layers) directions. In this analysis, to minimize effects due to different degrees of structural relaxation (see below), harmonic restraints with a force constant of 1000 kJ/mol·nm² are applied to all atoms in the filament to maintain the structure to be close to the initial EM structural model during the MD simulation; the final RMSD is 0.05 nm after 10ns. While the simulations are conducted with explicit solvent, only inter-peptide interactions are computed without water for this analysis; to approximately take the effect of solvation into consideration, a distance-dependent dielectric model is used.

As shown in Fig. S33, the neighboring peptides are mainly stabilized by van der Waals interactions; this is the case for both lateral and perpendicular pairs, and the magnitude of interaction is stronger for the perpendicular pairs due to favorable sidechain stacking interactions. In particular, as shown in Fig. S34, Phe sidechains of lateral neighbors form favorable van der Waals interaction, while  $\pi$ - $\pi$  stacking between aromatic sidechains and hydrogen bonds among peptide bonds stabilize vertical pairs. There is considerable amount of electrostatic repulsion between the lateral pair of NBD residues and the perpendicular pair of methylated lysine residues; the electrostatic repulsion between NBD residues suggests that water molecules and/or ions are likely present in the core of the filament to provide stabilizing interactions. Overall, when the fluctuations among different snapshots are considered, there is no significant difference between the *cis* and *trans* filament models in terms of peptide-peptide interactions, at least when the structure remains close to the EM structural model.

#### Note S2. Extension and water content of the filament

As discussed in the main text, the filament elongates and takes up water molecules during MD simulations. To quantify the number of water molecules and ions that are absorbed in the filament ( $N_{\text{wat}}$ ,  $N_{\text{ion}}$ ), we calculate the distance between an ion or a water oxygen and the nitrogen atom of a nitro group in NBD (Fig. S35). If the minimal distance is less than 0.5 nm, the ion or the water molecule is considered as adsorbed.

We monitor the length of the filament  $(L_z(t))$ , the number of water and ions at the core region of the filaments  $(N_{wat}, N_{ion})$  as functions of simulation time in all model systems studied (Fig. S36). The results show several trends.

First, focusing on the 1-KMe $_3$  fiber, it is clear that the *cis* model deviates further from the initial EM structural model compared to the *trans* model; this is particular the case with low fion, although the difference between them gets smaller as fion increases. In fact, the *cis* and *trans* models exhibit different trends with respect to fion; the *cis* model appears to be stabilized by the ions in the center, while the *trans* model is most stable with small values of fion. Nevertheless, in all fiber models (except obviously for fion=0), the number of ions in the core decreases during the simulation and reaches a plateau value of ~5, suggesting that a modest number of ions feature favorable interactions with the core residues.

Second, the number of water molecules inside the filament increases rapidly during the simulation, although the water molecules initially placed in the core diffuse away from the fiber (data not shown); evidently, there is extensive water exchange between the interior of the filament and the bulk. Consistent with the smaller degree of length extension, the *trans* fiber contains a lower number of internal water molecules with most f<sub>ion</sub> values.

Finally, comparing 1-KMe<sub>3</sub> and 1P-KMe<sub>3</sub>, it is evident that the magnitude of extension is larger for the latter, for both the *cis* and *trans* models and all f<sub>ion</sub> values. Correspondingly, the number of water molecules adsorbed into the fiber is substantially larger for 1P-KMe<sub>3</sub>. These trends are consistent with the notion that the phosphorylated form of the fiber is less stable.

### Note S3. Quantification of filament bundling in CG simulation

To monitor the equilibration of the CG simulations, we calculate the rotational correlation function  $U(t) = \langle u(t) \cdot u(0) \rangle / |u(0) \cdot u(0)|$ , where u(t) is the end to end vector of a polymer at time t. The rotational relaxation time  $\tau$  is then defined as the time that  $U(\tau)$  first reaches ~1/e. To calculate  $\tau$ , we monitor a single polymer in a system with media of various crowder volume fraction  $\rho$ . As shown in Fig. S37a,  $\tau$  ranges from 2,000 to 3,000 and increases slightly as a function of  $\rho$ . Thus we perform filament bundling simulations for up to 50 $\tau$  to ensure that the system reaches equilibrium.

To quantify the formation of polymer bundle, we calculate the radial distribution function g(r) for polymer monomers. When the polymers remain separated in the solution phase, the height of the first peak of g(r) is less than 2. On the other hand, when polymer bundles are formed, the height of the first peak increases to be more than 100 (Fig. S37b). By measuring the height of the first peak of g(r), we can differentiate between polymer solution and bundled phases.

## Note S4. Bundling of Filaments Depends on Stickiness and Volume Fraction of Crowders

There are three physical parameters that affect the bundling of polymer chains - the stiffness ( $k_{angle}$ ) of the polymer chain<sup>4-6</sup>, and interaction strength between monomers ( $\epsilon = k_B T$ )<sup>6</sup>, and volume fraction of crowders<sup>7-10</sup>. All three factors contribute positively to the probability of bundle formation (Fig. S38). Previous studies found that when the stiffness of polymer is not sufficiently high, it is difficult to form bundles<sup>6</sup>. This observation is confirmed here; when  $k_{angle}$  is less than 150  $k_B T/\theta_0^2$ , bundles do not form even with high  $\epsilon$  and  $\rho$ . Therefore, we choose a high value for  $k_{angle}$ (300  $k_B T/\theta_0^2$ ), and primarily explore the impact of  $\epsilon$  and  $\rho$  on the bundling behavior. The results are summarized in the phase diagram shown in Fig. S39. Evidently, transition to the bundling phase is sensitive to the monomer-monomer interaction; only for a fairly narrow range of  $\epsilon$  values, the bundling of polymers depends sensitively on the crowder density.

# Supplemental Tables

Table S1. Cryo-EM data collection, refinement and validation statistics

	1-KMe <sub>3</sub> type 1 filament (EMDB-XXXX) (PDB XXXX)	1-KMe <sub>3</sub> type 2 filament (EMDB-XXXX)
Data collection and processing		
Magnification	130,000	130,000
Voltage (kV)	300	300
Electron exposure (e/Å <sup>2</sup> )	20	20
Defocus range (μm)	-1.5 to -2.5	-1.5 to -2.5
Pixel size (Å)	1.06	1.06
Symmetry imposed	Helical (rise 4.9 Å, twist 2.3°)	Helical (rise 4.9 Å, twist 2.7°)
D (1)	C7	C2
Particle segments (no.)	108,886	65,221
Map resolution (Å)		27.4
model:map FSC (0.38)	4.3	N.A.
$d_{99}$	4.2	5.0
Refinement		
Map sharpening B factor ( $Å^2$ )	-100	-100
Real space correlation coefficient	0.7	N.A.
Clash scores	16.2	N.A.

Table S2. Summary of MS (ESI) results of compounds

Name	Calc.	Obsvd. [M] <sup>+</sup> or [M-H] <sup>+</sup>
1P-KMe <sub>3</sub>	960.96	960.43
2P-KMe₃	960.96	960.23
3P-KMe₃	960.96	960.36
1P-K	917.87	918.43

Table S3. Eluting gradient for HPLC

Time (minute)	Flow (ml/min.)	H <sub>2</sub> O %	Acetonitrile %
0	10	70	30
15	10	30	70
16	10	0	100
18	10	0	100
19	10	70	30
22	10	70	30

Table S4. Summary of atomistic MD simulations.

Composing Peptide	Peptide Configuration	Number of Independent Simulations	Simulation Length (ns)
1-KMe <sub>3</sub>	Cis	3	120
	Trans	3	120
1P-KMe <sub>3</sub>	Cis	3	120
	Trans	3	120

<sup>&</sup>quot;Cis" and "Trans" indicate the configuration for the peptide bond that connects NBD and Phe. For each filament model, four different initial placements of  $Na^+$  ions in the filament core ( $f_{ion}$  = 0, 0.5, 0.72 and 1.0) are tested.

## Supplemental references

- 1. E. A. Ottinger, L. L. Shekels, D. A. Bernlohr, G. Barany. (1993). Synthesis of phosphotyrosine-containing peptides and their use as substrates for protein tyrosine phosphatases. Biochemistry *32*, 4354-4361.
- R. Baba, Y. Hori, S. Mizukami, K. Kikuchi. (2012). Development of a Fluorogenic Probe with a Transesterification Switch for Detection of Histone Deacetylase Activity. Journal of the American Chemical Society 134, 14310-14313.
- 3. Y. B. Cai, Y. Shi, H. M. Wang, J. Y. Wang, D. Ding, L. Wang, Z. M. Yang. (2014). Environment-Sensitive Fluorescent Supramolecular Nanofibers for Imaging Applications. Analytical Chemistry *86*, 2193-2199.
- 4. J. P. K. Doye, R. P. Sear, D. Frenkel. (1998). The effect of chain stiffness on the phase behaviour of isolated homopolymers. J Chem Phys *108*, 2134-2142.
- 5. J. Zierenberg, W. Janke. (2015). From amorphous aggregates to polymer bundles: The role of stiffness on structural phases in polymer aggregation. EPL *109*,
- 6. D. C. Lee, G. Kwon, H. Kim, H. J. Lee, B. J. Sung. (2012). Three-dimensional Monte Carlo simulation of the electrical conductivity of carbon nanotube/polymer composites. Appl. Phys. Express *5*,
- 7. L. A. Munishkina, E. M. Cooper, V. N. Uversky, A. L. Fink. (2004). The effect of macromolecular crowding on protein aggregation and amyloid fibril formation. J. Mol. Recogn. *17*, 456-464.
- 8. K. Richter, M. Nessling, P. Lichter. (2008). Macromolecular crowding and its potential impact on nuclear function. Biochim. Biophys. Acta Mol. Cell Res. *1783*, 2100-2107.
- 9. M. D. Shtilerman, T. T. Ding, P. T. Lansbury Jr. (2002). Molecular crowding accelerates fibrillization of α-synuclein: Could an increase in the cytoplasmic protein concentration induce Parkinson's disease? Biochemistry *41*, 3855-3860.
- 10. Y. Hata, T. Sawada, T. Serizawa. (2018). Macromolecular crowding for materials-directed controlled self-assembly. J. Mater. Chem. B *6*, 6344-6359.

Supplemental Videos and Spreadsheets

Click here to access/download **Supplemental Videos and Spreadsheets**Movie S1.mp4

Supplemental Videos and Spreadsheets

Click here to access/download **Supplemental Videos and Spreadsheets**Movie S2.avi

Supplemental Videos and Spreadsheets

Click here to access/download **Supplemental Videos and Spreadsheets**Movie S3.avi